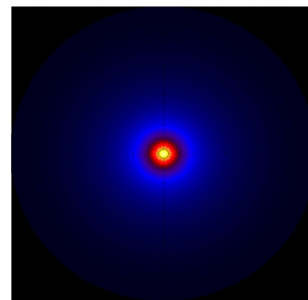
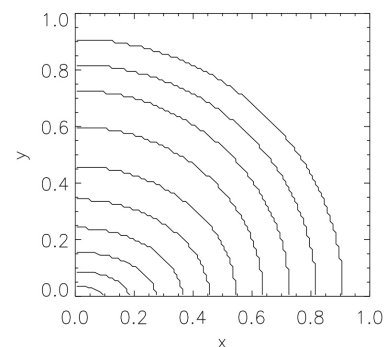
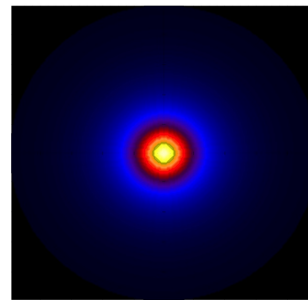
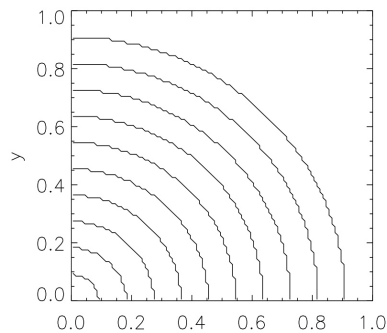


The Shape of Galaxy Clusters



A thesis submitted for the degree of
M.Sc. Physics
on December 15, 2010.

Martina Zamboni

Supervisor: Steen H. Hansen

Dark Cosmology Centre, Niels Bohr Institute
Faculty of Science, University of Copenhagen

Acknowledgements

This thesis has been written between November 2009 and December 2010 at the Dark Cosmology Center. It has been a long (and sometimes hard) year and I want to thank everyone for their support and patience. I haven't been home for twelve months, relocated seven times, travelled 5000 km by train and camped in a island above the Arctic Circle. In the time between, I also learned something about Astrophysics. I am much better at debugging and moving boxes now, and I am grateful to whoever has helped me with both.

First of all, I want to thank my supervisor Steen, for good ideas and good humor, and for never pointing out that I sometimes avoid him in the hallways. Thanks to Signe, who let me used the data; Andreas, who helped me coding and introduced me to a social network for programmers; Teddy, who explained me the many wonders of cosmomc; Johan for sharing views on Xspec. A big thank you to Karen for taking the time to proofread. I thank everyone at Dark, for making it the great place it is (I will miss you all!). I am grateful to the administrators of the Stefan Rozental og Hanna Kobylinsky Rozentals Fond for deciding that this project was worth funding and to the Dark Cosmology Center for some extra funding.

I also want to thank my family, for their crucial role in mailing me copies of Elle Italy every month, and all my friends in Denmark, Italy or anywhere else in the world. Finally, I owe many thanks to Alberto, whose name should probably be credited on the first page of this work.

Abstract

Galaxy clusters are the biggest structures in the universe to have reached equilibrium. Their properties are expected to reflect the properties of the universe as a whole and, for this reasons, clusters are often used as cosmological laboratories. Observations tell us that most clusters look elliptical in the sky but, surprisingly, there is no satisfactory way to know their 3D structure, that is usually approximated to a simple spherical model. A better knowledge of the true structure would affect the cluster mass and, therefore, the determination of the cosmological parameters.

We present here a new method to reconstruct the full 3D shape of a cluster, using X-rays observations only. This is done following two different approaches: 1) The first method is an extension of an existing technique, known as deprojection, which is used to recover the 3D temperature and density profiles of the intracluster medium. Here we extend the deprojection to the more general non-spherical case and apply it to a number of simulated clusters as well as to observations of A2218 and A1689. Simulations prove that the effect is indeed detectable, although it's difficult to constrain in the case of a cool-core cluster. 2) In the second part, we start from a theoretical model of a non-spherical cluster and use a Monte Carlo method to make a fit to the observations.

Contents

1	Clusters of galaxies	5
1.1	The formation of structures	6
1.2	Observations of clusters	7
1.3	Cluster cosmology	9
1.4	Why not spherical?	10
1.5	Clusters in X-rays	11
1.6	Clusters in Microwave	14
1.7	From X-rays observations to mass	17
2	Observations	19
2.1	X-ray Observatories	20
2.2	Instrumental response	21
2.3	Theoretical emission model	24
3	Onion Peeling	26
3.1	From 3D to 2D...	27
3.2	...and back to 3D	27
3.3	The geometrical deprojection	28
3.4	Playing with the shape	30
3.5	Cell volumes	32
3.6	Modeling the intracluster medium	34
3.7	A toy model	35
3.8	β -model	39
3.9	Cool core clusters	41
3.10	Abell 1689	46
4	A Monte Carlo approach	50
4.1	Monte Carlo methods	51
4.2	CosmoMC	52
4.3	Calculating the spectrum	54

4.4	Testing	59
4.5	What's next?	60
	Appendices	64
A	Deprojection of Abell 2218	64
B	Extracting the response files	66
B.1	The spectral response	66
B.2	The ancillary response	68
C	The Hubble constant	69
D	My code	72
D.1	Deprojection	72
D.2	Projections and Monte Carlo	73
D.3	Response matrices	74

CHAPTER 1

Clusters of galaxies

GALAXIES ARE NOT SPREAD evenly in the universe. Most of them can be found in large collections called clusters, where hundreds of galaxies are held together by gravitational attraction. Clusters can be as massive as $10^{15}M_{\odot}$, which makes them the largest equilibrated objects in our universe [8]. A typical cluster size is of the order of several megaparsec.

Clusters of galaxies might have been called something different if they had first been discovered in a waveband other than optical light, because the hundreds to thousands of galaxies in a cluster only make up a few percent of the total cluster mass (5 – 10%). At least the same amount of matter exists in the form of X-ray luminous hot gas that fills up the space between galaxies. The remaining 80% of the mass is not directly detectable, as it does not emit light, and can only be observed through its gravitational effects. Its properties must be linked to the universe we observe today: element abundance, structures such as galaxies and clusters, stellar formation history, energy density, etc. The exact identity of dark matter particles remains a mystery, although there are several possible candidates.

1.1 THE FORMATION OF STRUCTURES

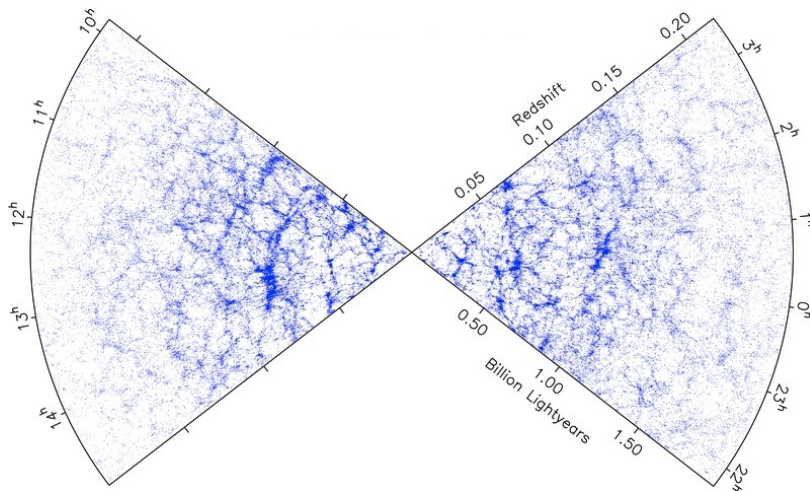


Figure 1.1: A slice of the universe as reconstructed from a redshift survey. The survey maps the distribution of matter within a section of the sky, by combining redshift and angular position data. The figure shows the large scale structure of the universe, made up of clusters, filaments and voids [15].

The simplest cosmological model predicts a single species of cold dark

matter particles (CDM), that clusters at small scales. According to this model, large scale structures are the result of a bottom up process, with smaller objects coming first, while the largest objects, such as superclusters, are still assembling.

The matter that goes on to form a cluster initially begins as a low amplitude perturbation in the density distribution of the dark matter. Regions whose density slightly exceeds the mean density are gravitationally bound and decouple from the expansion, collapsing on themselves in a small clump. Because density perturbations are bigger on small scales, small objects are the first to collapse. These small objects collect into galaxies, and galaxies then collect into clusters. Therefore the largest structures, like clusters, are also the last to approach an equilibrium configuration and their growth should directly trace the process of structure formation in the universe.

A cluster in equilibrium is characterized by a virial relation:

$$E_{kinetic} = -2E_{potential} \propto \frac{GM}{R} \quad (1.1)$$

where the mass, M , is the total gravitating mass of the cluster, including gas, stars and dark matter.

1.2 OBSERVATIONS OF CLUSTERS

Clusters of galaxies were first optically identified by the end of the eighteenth century. Optical discoveries continued to accumulate as the observing power grew over the next two centuries, culminating with the semi-definitive catalog of George Abell and collaborators [2], which contains most of the known nearby galaxy clusters, up to a nominal redshift of $z = 2$. Clusters are found by optical or infrared telescopes by searching for over densities, and then confirmed by finding several galaxies at a similar redshift. Individual clusters can be studied in detail using a number of observational techniques:

- **X-rays.** Since the hot intracluster gas is an incredibly bright X-ray source, X-ray spectroscopy is the ideal tool to obtain information on the the intracluster medium and generally on cluster properties [45]. The next few sections contain an overview of the main properties of X-rays from galaxy clusters (see Section 1.5).

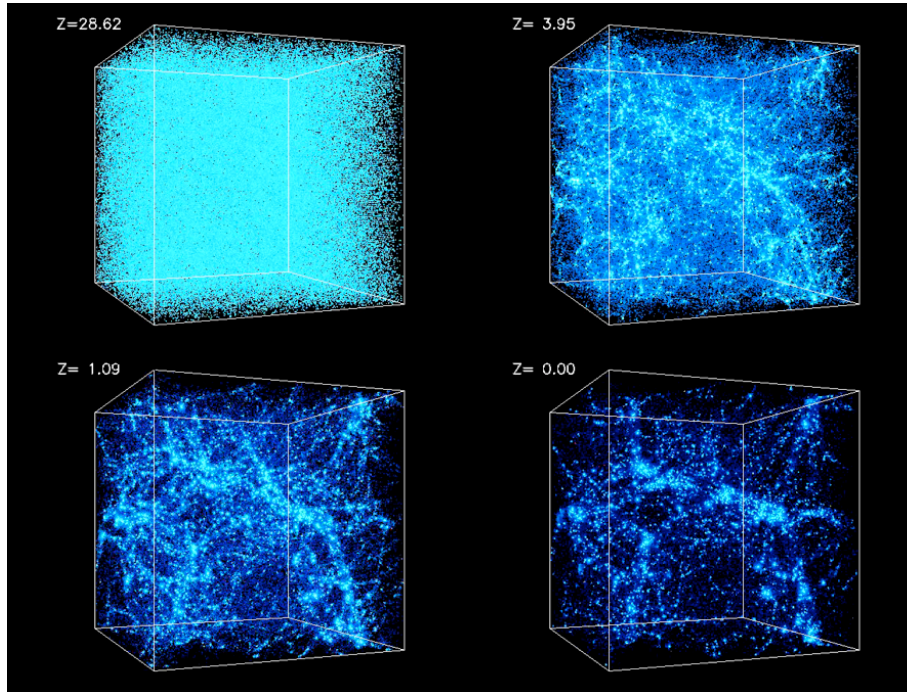


Figure 1.2: The movie stills pictured above illustrate the formation of clusters and large-scale filaments in the cold dark matter model with dark energy. At early times (*top left*) distribution of matter appears to be uniform. This is because the seed fluctuations are still fairly small. As time goes on, the fluctuations grow resulting in a wealth of structures from the smallest bright clumps which have sizes and masses similar to those of galaxies to the large filaments (*bottom right*) [12].

- **Microwaves.** The hot gas can be observed also through its effect on the cosmic microwave background (CMB). Compton scattering of the CMB photons by electrons in the intracluster medium produces a shadow in the CMB: this effect is known as Sunyaev–Zel’dovich (SZ) [48].
- **Gravitational lensing.** The gravitational field of a galaxy cluster bends the space-time, so that photons approaching the cluster travel on curved paths. The effect is strong enough that we see a distortion in the background distribution of galaxies (in this sense, the cluster is acting like a lens). Observations of this effect provide information on the distribution of matter in the cluster [8].

Besides, we can successfully extract new information by combining different methods: for instance, a combination of X-rays and SZ maps yields a direct



Figure 1.3: The galaxy cluster Abell 1689 at optical wavelengths as seen by Hubble Space Telescope (*NASA*, 2007). The long arcs in the image are caused by gravitational lensing of the background galaxies by matter in the cluster.



Figure 1.4: Another image of A1689 with the X-ray emission shown in purple. Composite of data from the Chandra X-ray Observatory (in purple) and the Hubble Space Telescope (in yellow). Credit: *X-ray: NASA, CXC, MIT, Peng et al. Optical: NASA, STScI.*

measurement of the Hubble constant (see Chapter 1.6). It is also common to give a joint mass estimate from X-ray and lensing data (Chapter 1.7). This work, however, is mainly focused on X-ray observations and their relation to the cluster's shape. The biggest advantage of using a single technique is that only one data set is required and it is easier to keep track of the observational errors.

1.3 CLUSTER COSMOLOGY

There are two features of clusters that make them so useful when it comes to study cosmic evolution. First, clusters are the biggest objects whose masses we can reliably measure, because they are the largest structures who have undergone relaxation and entered into virial equilibrium. Second, clusters are essentially closed systems, whose composition should be well representative of the universe as a whole [52]. In particular, the ratio between baryons and dark matter in massive clusters is expected to be

constant and closely match the global ratio of the universe.

One should, however, be careful when deriving the cluster mass or other properties from the observables. At some point, it is required that we make some assumptions on the three-dimensional shape of the cluster (which is unknown). For convenience of the calculations, and perhaps lack of a better model, it's common to describe clusters as spherical systems.

1.4 WHY NOT SPHERICAL?

Symmetrical structures are not what we usually see in the sky: instead, clusters surveys tell us that most clusters are not at all spherical, but rather look like triaxial ellipsoids [40, 44]. Even a cluster that appears circular in the sky –something astronomers are eager for, as it may indicate an old, virialized structure– could, in principle, not be spherical at all, but just a spheroidal structure which we happen to observe under the right angle.

In fact, there are strong suggestions that this might be the case at least for a famous, circular looking clusters: Abell 1689. This cluster is well known for its amazing system of gravitational arcs, one of the largest ever observed (see the bright arcs in Figure 1.3), and its great number of multiple images. A1689 has a smooth, symmetrical X-rays emission, and for this reason it has been proposed as a standard example of spherical cluster in hydrostatic equilibrium [34, 53]. However, later studies have found large discrepancies in mass estimates obtained from gravitational lensing and X-rays observations [5, 31]. Since the lensing signal probes the integrated mass along the line of sight, it is sensitive to the elongation of the cluster and such discrepancies could be interpreted as suggestions that A1689 might actually have a prolate shape, which is, by coincidence, aligned with the line of sight [5, 16, 22].

In cases like this, we expect the X-ray emission from a prolate gas distribution to be slightly different from a spherical one. A prolate cluster tends to give a higher central surface brightness than other distributions where the same mass is spherical or oblate. In this sense, X-ray observations could be used to discriminate between different geometries, unveiling the true shape of the cluster. In this thesis, I will present and discuss a new method to find the true ellipticity of a cluster that is based on its X-rays emission only.

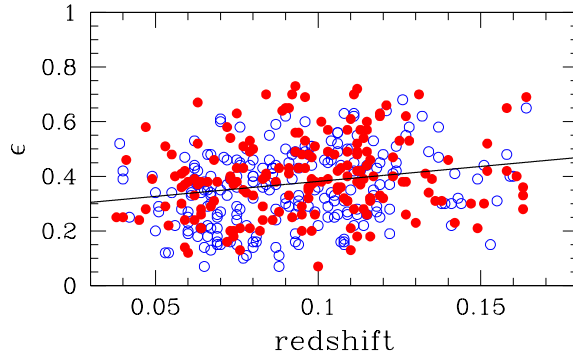


Figure 1.5: Evolution of the mean cluster ellipticity with redshift. Open circles represent clusters from the APM survey, filled circles are Abell clusters. Figure from Plionis, 2002 [40]. Similar results are found in numerical simulations [23].

1.4.1 ELLIPTICITY AS A COSMOLOGICAL PROBE

The use of ellipticity as a tool to constrain the cosmological parameters has been investigated using optical and X-rays clusters samples [40], as well as in large scale cosmological simulations [23]. The results agree that the mean ellipticity of clusters increases monotonically with redshift, suggesting that clusters were more elliptical at earlier times. As time goes by, they relax towards an equilibrated configuration, becoming more and more and spherical (Fig. 1.5); the dependence is stronger for massive clusters.

The cosmological parameter that shows the biggest dependence on the ellipticity is the amplitude of the initial fluctuations, σ_8 [23]. Higher values of σ_8 (i.e., clusters are forming earlier) lead to lower mean ellipticities at present time. Results from numerical simulations should be compared with observations of large samples of clusters, to give new constraints on the cosmological parameters.

1.5 CLUSTERS IN X-RAYS

X-ray observations reveal that clusters are filled up with hot, dilute gas, that has been heated up to temperatures of $T \approx 10^8$ K or several keV per particle [45]. At such temperatures the light elements are completely ionized and the radiation results from collisional interactions between electrons and ions. This mechanism is discussed in details in Chapter 1.5.1

The gas is so hot because it is compressed within the deep potential well of the cluster. Similarly to the virial equilibrium of galaxies and dark matter

particles, the gas thermalizes and heats up to a temperature that reflects the depth of the surrounding gravitational potential [50]. In a relaxed cluster, the intracluster medium is close to the hydrostatic equilibrium and the plasma temperature inferred by X-rays is related to the cluster mass (see Chapter 1.7).

The rate at which the gas radiates energy in the X-ray, or emissivity (per unit volume), depends on the electron temperature, T , and is proportional to the squared electron density n_e^2 ,

$$\epsilon_X \propto n_e^2 \Lambda(T) \quad (1.2)$$

A detailed description of the emission mechanism is provided in Section 1.5.1.

The density dependence makes it difficult to measure the emission from the outer part of the cluster, where n_e can be as low as 10^{-5} cm^{-3} and the X-ray flux becomes extremely faint. X-rays observations are usually confined well within r_{500} , the radius at which the mean cluster density is 500 times the critical density.

The dependence on the temperature is more complex, but the most important feature is a sharp cut-off of the spectrum at high energy, due to an exponential term with argument $-E/T$. The quantity $\Lambda(T)$ is known as the cooling function, and can only be computed numerically in most cases. The specific code I have used is the *mekal* implemented in Xspec (see Chapter 2.3.1), which requires that the gas is isothermal and the metallicity is known.

Another useful quantity is $EI \equiv \int n_e^2 dV$, known as emission integral, which gives the normalization of the spectrum¹.

A note on the low density

The plasma density is so low that most of the photons don't experience further interactions and leave the cluster unchanged. This means that the spectrum we observe from a galaxy cluster provides an account of the entire intracluster medium: this is different from, e.g. the spectra of stars, that merely provide information on a thin skin on their surface. The gas is also sufficiently transparent that the transfer of radiation can be neglected [37]. This is another reason why cluster X-ray spectra are so straightforward to interpret.

¹This definition is not unique, and the emission integral is sometimes defined as $\int n_H n_e dV$, where n_H is the number of hydrogen nuclei. Throughout this work I assume a fully ionized plasma where the relative elemental abundance gives $n_e = 1.2n_H$ [11].

1.5.1 EMISSION MECHANISM

With extremely high temperatures and low density, the intracluster medium can be well described as an ideal gas, making the physics behind the X-ray emission easy to model.

For typical cluster temperatures ($kT > 2\text{keV}$ per particle) the emissivity of thermal bremsstrahlung dominates that from emission lines. The situation is reversed at lower temperature (below 2 keV): the heavy elements are not fully ionized and line emission becomes important [11].

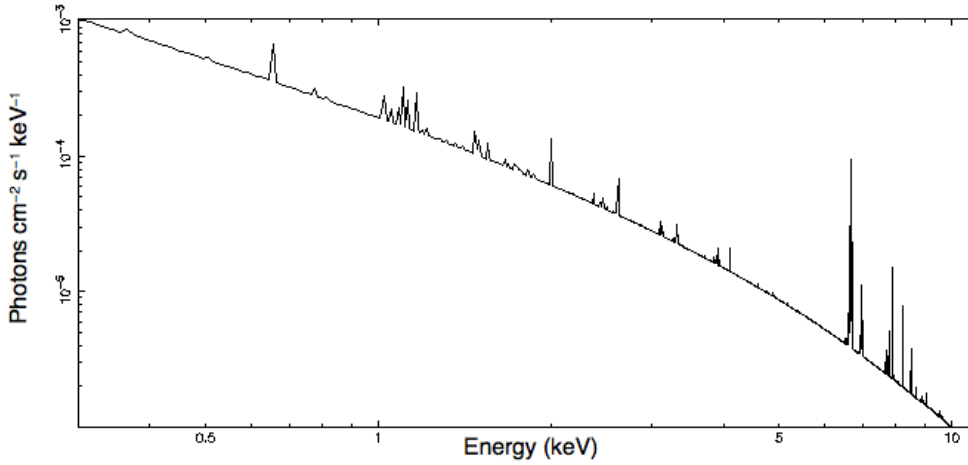


Figure 1.6: Example of X-ray emission from a plasma at 5keV and 0.3 solar abundance. The smooth continuum is the contribution from bremsstrahlung, which is the dominant process at such temperature. Several transition lines are visible: the bright group of lines around 7keV is the Iron and Nickel blend.

Bremsstrahlung

The fundamental emission process is bremsstrahlung², or free–free emission, which happens when a charged particle, like an electron, is deflected by the encounter with another charged particle. The spectral energy distribution for a single temperature plasma of Maxwellian particles is given by [45]:

$$e(\nu) = \frac{16\pi e^6}{3m_e c^3} \left(\frac{2\pi}{3m_e k} \right)^{1/2} Z^2 n_e n_H g_{ff}(Z, T, \nu) T^{-1/2} e^{-\frac{h\nu}{kTg}} \quad (1.3)$$

²From German: braking radiation.

for collisions with an ion of charge Z . The Gaunt factor g_{ff} is a small quantum mechanical correction that needs to be computed numerically, but is usually a number close to one [47].

The part of the spectrum due to bremsstrahlung is known as the continuum. The main feature of the continuum is the exponential tail, whose intensity goes as $e^{-\frac{E}{T}}$ [45]. As long as this cut-off is seen in the energy window of the telescope, one has a good handle on the temperature measurement.

Line features

Abundances of elements are relatively easy to measure from the emission lines, as long as the temperature of the gas is well defined. The main line feature is a blend of lines from iron and nickel at energies between 6.5 and 7 keV, usually known to as the ‘7 keV iron line’ (Figure 1.6). If the shape of the continuum is used to derive a temperature, then the width of the lines gives a measure of the abundance of iron (and heavy elements) in the gas. On average, abundances in clusters are 0.3 times the solar abundance [45].

1.6 CLUSTERS IN MICROWAVE

The presence of hot gas can be observed as it induces a slight depression in the temperature of the cosmic microwave background at the locations of clusters. This happens when a CMB photon traveling through the cluster gets Compton scattered off the hot electron gas. As its momentum is slightly increased, the photon gets shifted to higher energies, and we can see a distortion on the otherwise uniform microwave background. The effect appears as a decrement in the Rayleigh-Jeans part of the spectrum ($h\nu \ll kT$), and an increment on the Wien side ($h\nu \gg kT$). These results were predicted in the 70s by the Russian physicists Sunyaev and Zel’dovich [48]. This intensity change in the CMB radiation is proportional to the integral of the electron pressure along the line of sight,

$$y = \frac{k_B}{m_e c^2} \sigma_T \int n_e T_e dl \quad (1.4)$$

which is also known as the ‘Comptonization parameter’ [48]. Here, T_e and n_e indicate, as usual, electron temperature and density, while σ_T is the Thomson scattering cross section. Even for the richest, and most luminous galaxy clusters the effect is small, with the overall change in brightness of

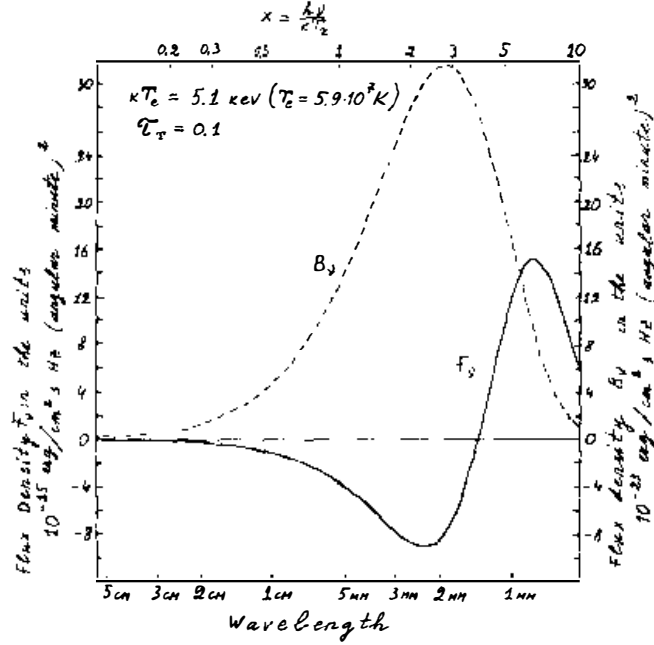


Figure 1.7: A drawing of Sunyaev illustrating the eponymous effect [48]. The solid line is the distortion in the CMB spectrum in the direction of a cluster of galaxies of $kT_e = 5.1\text{keV}$ as a function of wavelength. The blackbody spectrum is shown for comparison on a different scale (broken line).

the CMB being of about 1 part in 10^4 . Detecting such a small change requires very sensitive, low noise observations. Nowadays, there are accurate measurements of the SZ effect in several clusters [9].

The Sunyaev-Zel'dovich effect does not depend on the redshift, i.e. the change in brightness of the CMB radiation due to the presence of a cluster can be seen at all positions on the line of sight. Thus, an accurate SZ cluster survey can efficiently find objects out to high redshifts, observing distant clusters of galaxies whose X-ray flux is difficult to detect (if not impossible).

A comparison of the SZ map and X-ray image of a cluster can be used to derive interesting information about the structure of the gas, in particular, it might be used to determine the intrinsic three-dimensional shape of the cluster.

1.6.1 THE HUBBLE CONSTANT

The Sunyaev-Zel'dovich effect offers the possibility to measure directly the distance to a galaxy cluster, bypassing the standard distance ladder. Even better, it provides us with an independent estimate of the Hubble constant H_0 . This method is discussed in detail in Appendix C, but the basic idea is that the SZ effect and the X-ray emission from the same cluster scale differently with the gas density and the line-of-sight size of the cluster.

The SZ effect depends on average electron pressure, $n_e T_e$, integrated along the line of sight

$$\Delta T \propto \int n_e T_e dl \quad (1.5)$$

while the X-ray observable, that is the surface brightness, scales as the density square,

$$S_X = \frac{d_A}{4\pi(1+z)^3} \int n_e^2 \Lambda_e dl \quad (1.6)$$

Assuming that clusters are spherical objects with smooth gas distributions, the dependence on n_e can be eliminated by a combination of (1.5) and (1.6), deriving the line-of-sight thickness of the cluster, l . If the cluster is indeed spherical (note that this is the crucial assumption), from a comparison with its apparent angular size, θ , we can directly estimate the cluster angular diameter distance, $d_A = \frac{l}{\theta}$, which can be used to find the Hubble constant, once the values of the cosmological parameters are specified (Fig. 1.8a).

This method relies on very simple physics (the properties of a ionized gas in quasi-equilibrium), but it requires that we know the length of the path through the gas, in order to evaluate correctly the integrals in (1.5) and (1.6). A result by Birkinshaw et al. [10] shows that a prolate cluster, with the line-of-sight dimension being q times longer than the radial dimension, will affect the measure of d_A , and hereby H_0 , by a factor $1/q$:

$$d_A(true) = \frac{d_A(estimated)}{q} \quad (1.7)$$

A study of high redshift galaxy cluster CL 0016+16 by Hughes and Birkinshaw [24] quantifies the uncertainty on H_0 from the unknown geometry to be at least 15% (Fig. 1.8b). This makes it clear that, to use this method effectively, it's important that we know something about the three-dimensional shape of the cluster.

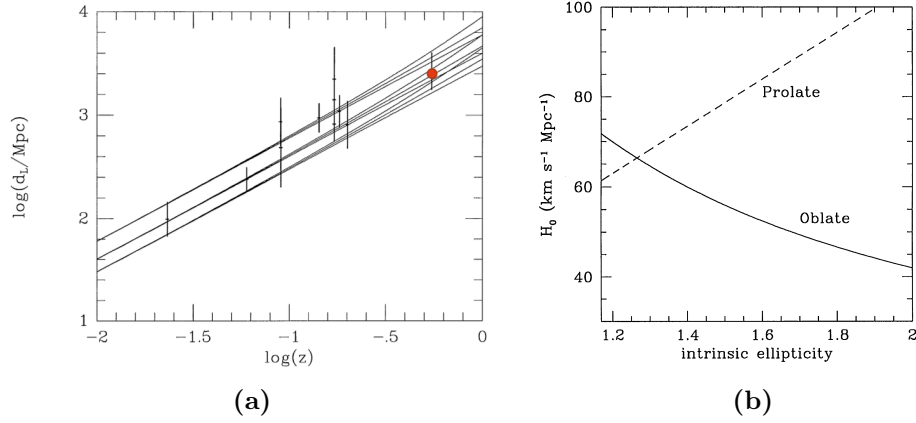


Figure 1.8: (a) A Hubble diagram based on the distance measured for nine Abell clusters and the distant cluster CL 0016 + 16 (red dot) [9]. The best fit is for a Hubble constant of about $60 \text{ km s}^{-1} \text{ Mpc}^{-1}$; however, the uncertainty deriving from the cluster shape has not been taken into account. (b) Variation of the value of the Hubble constant with the axis ratio of the distant galaxy cluster CL 0016+16 for oblate and prolate geometries, assuming cluster symmetry in the plane of the sky [24]. The error on H_0 associated with the unknown geometry is estimated to be around 15%.

1.7 FROM X-RAYS OBSERVATIONS TO MASS

The density and temperature distributions of the X-ray gas within galaxy clusters can be used to estimate the total mass of the cluster, under the assumption of hydrostatic equilibrium. This approximation is reasonable as long as the cluster is stationary (the gravitational potential doesn't change with time) and gas motions are subsonic [45, 46]. In this way, the only force acting against the gravitational pull is thermal pressure.

Assuming the gas is in equilibrium in the cluster potential well, the gas pressure is related to the potential by [45]

$$\nabla P = -\rho_g \nabla \phi \quad (1.8)$$

where P is the gas pressure; ρ_g is the gas density and ϕ is the gravitational potential of the cluster. As seen in 1.5, the intracluster medium is an ideal gas. Its equation of state $P = P(\rho)$ is

$$P = \frac{\rho_g T}{\mu m_p} \quad (1.9)$$

where $\mu \approx 0.63$ is the mean atomic weight of the gas in units of the proton mass, m_p , and is constant throughout the cluster.

The hydrostatic equilibrium tells us how much gravity is needed to prevent the gas from blowing away: its pressure must be balanced by an inward pull, provided by gravity. If the gas distribution is spherical, equation 1.8 reduces to

$$\frac{dP}{dr} = -\rho(r) \frac{GM_{tot}(r)}{r^2} \quad (1.10)$$

It should be stressed that $M_{tot}(r)$ is a measure of all the gravitating mass within a sphere of radius r : stars, gas and dark matter.

Combining eq. 1.9 and eq. 1.10 gives

$$M(r) = -\frac{T}{G\mu m_p} r \left[\frac{d \log \rho_g}{d \log r} + \frac{d \log T}{d \log r} \right] \quad (1.11)$$

and the mass density can be determined if we know temperature and density of the intracluster gas [45]. Note that the mass depends weakly on the gas density (only through logarithmic derivatives), but strongly on the gas temperature. Also, the mass determination will only be as precise as the derivatives. A way to recover the density and temperature profiles is presented in Chapter 3.

There are other methods for measuring cluster masses: from velocity dispersions of cluster galaxies using the Jeans equation, and from gravitational lensing of background galaxies. The results from different methods have been found to be in disagreement for some clusters, which makes us question whether all the assumptions (hydrostatic equilibrium and spherical symmetry) hold true [5, 31]. If the mass distribution was other than spherical, this would directly impact on the mass estimate in 1.8, by deforming the shape of the gravitational potential, ϕ . Two famous controversial clusters are A1689 and A2218, whose case will be presented in Chapter 3.

CHAPTER 2

Observations

AS THIS WORK IS largely based on the analysis of X-rays observations, I think it's worth spending a few words introducing the telescope, the data format and the basics of spectral fitting in Xspec. I also introduce some technicalities related to the instrumental response files, that will be useful in Chapter 4.

2.1 X-RAY OBSERVATORIES

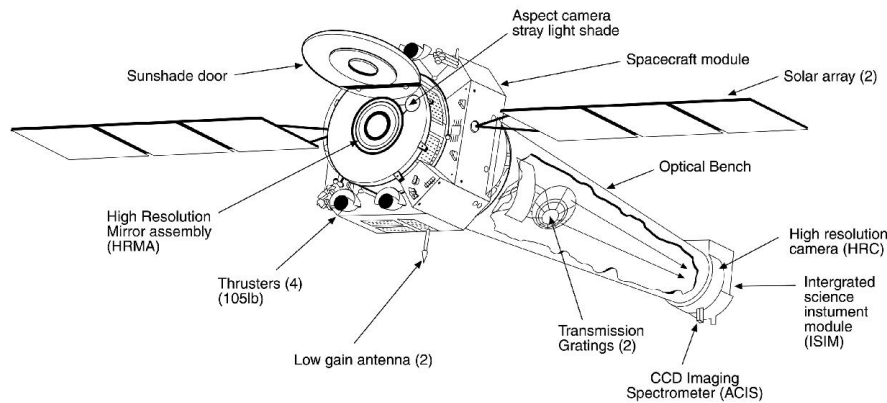


Figure 2.1: Schematic view of *Chandra* X-ray telescope. Image from *NASA, CXC, NGST*.

X-ray radiation is absorbed by the earth's atmosphere and therefore X-ray observations should be carried out onboard satellites. *Chandra* X-ray observatory (Fig. 2.1) was launched in 1999 and is the third of Nasa's great observatories in space¹, the others being Einstein and XMM-Newton. It was designed to provide high resolution imaging in the X-ray band, with a nominal resolution of about one arcsecond.

Chandra data are available at the Nasa's *Heasarc* archive [1]. The data files are in the FITS format, or 'flexible image transport system', which is the standard astronomical data format endorsed by Nasa [6]. I had access to two deep field observations of two galaxy clusters, Abell 1689 and Abell 2218, conducted with the imaging spectrometer ACIS-I (Table 3.1). The original data files were processed with *Chandra*'s observations analysis software (CIAO) for background subtraction and extraction of the instrumental response files. This work has

¹The telescope is named after the Indian physicist Chandrasekhar, who calculated the maximum mass for a white dwarf star and he did it all using hand-worked mechanical calculators - the famous Brunsviga machines.

been done by Signe Riemer-Sørensen, and a detailed description of the exact procedure can be found in her PhD thesis [43].

The data analysis has been largely done with Xspec, the package for spectral fitting provided by Nasa [6].

Cluster	Observation id.	Exposure time	Date	Detector
A1689	6930	77.15 ks	Mar 6, 2006	ACIS-I
A2218	1666	49.24 ks	Aug 30, 2001	ACIS-I

Table 2.1: Summary of *Chandra* observations.

2.2 INSTRUMENTAL RESPONSE

A quick glance at the data it's enough to realize that they do not quite resemble the theoretical spectrum (see Figure 2.3a and 2.3c). This is because the energy distribution of the photons collected by the CCD is not identical to the distribution of the incoming photons. All kinds of distortions induced by the detector go under the name of 'instrumental response', that combines a variety of factors, such as detector efficiency, energy resolution, transmission, vignetting, and more. In general, the response depends on the exact position relative to the center of the CCD and it might change with time in an unpredictable way, so that the exact calibration must be re-evaluated for every observation [42].

From a more abstract point of view, the response maps the spectrum from the energy space of the source to the detector channel space. Each response element, $R(i, E)$ is proportional to the probability that an incoming photon of energy E will be detected by the i -th channel [6]. If we observe a source of spectrum $f(E)$, the expected photon count within the instrument channel $C(i)$ will be

$$C(i) = \int_0^{\infty} f(E) R(i, E) dE \quad (2.1)$$

Ideally, we could invert equation (2.1) to obtain the actual spectrum of the source, but unfortunately, this is usually not feasible, as the inversion tends to be unstable to small changes in the count rate [6]. It is more straightforward to modify the theoretical predictions, trying to match the model spectrum to the data obtained by the spectrometer. For each theoretical spectrum $f(E)$, the predicted count $C(i)$ can be calculated from equation (2.1) and compared to the observed data.

2.2.1 CHANDRA'S RESPONSE FILES

For *Chandra* data, the response is stored in two files [6]:

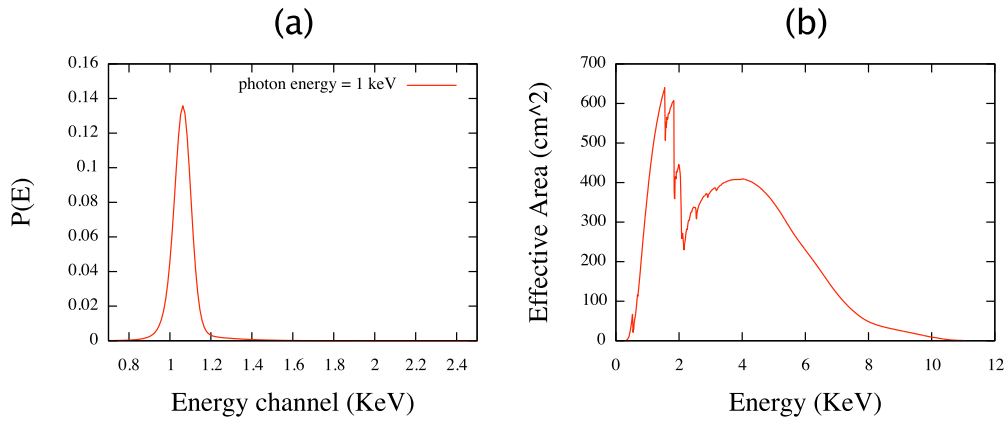


Figure 2.2: Response function of *Chandra* ACIS spectrometer. **(a)** Probability that a photon of energy 1 keV is detected by any of the CCD energy channels. The FWHM of the signal is the spectral resolution at the given energy, which is usually smaller at lower energies. This kind of information is stored in the redistribution matrix (*wrmf*). **(b)** Effective area, in cm^2 , vs energy of the ACIS-I spectrometer.

1. A **detector redistribution matrix** or *wrmf* describes the line broadening of spectral lines due to the detector resolution [21]. The *wrmf* consists of a compressed two-dimensional matrix, mapping from incident photon energy to instrument energy channel (Figure 2.3a).
2. An **ancillary response file** (*arf*) which describes the efficiency of the CCD and can be thought of as the transformation of a flat spectrum through the detector (Fig 2.3b). The ancillary response accounts for effective area of the telescope and collimator; vignetting; transmission effects and detector quantum efficiency. The *arf* is stored in a single one-dimensional array

The response matrices are stored in a compressed format where all the zero-elements have been removed, to minimize their size [21]. More details about *Chandra*'s response files follow in Appendix B.

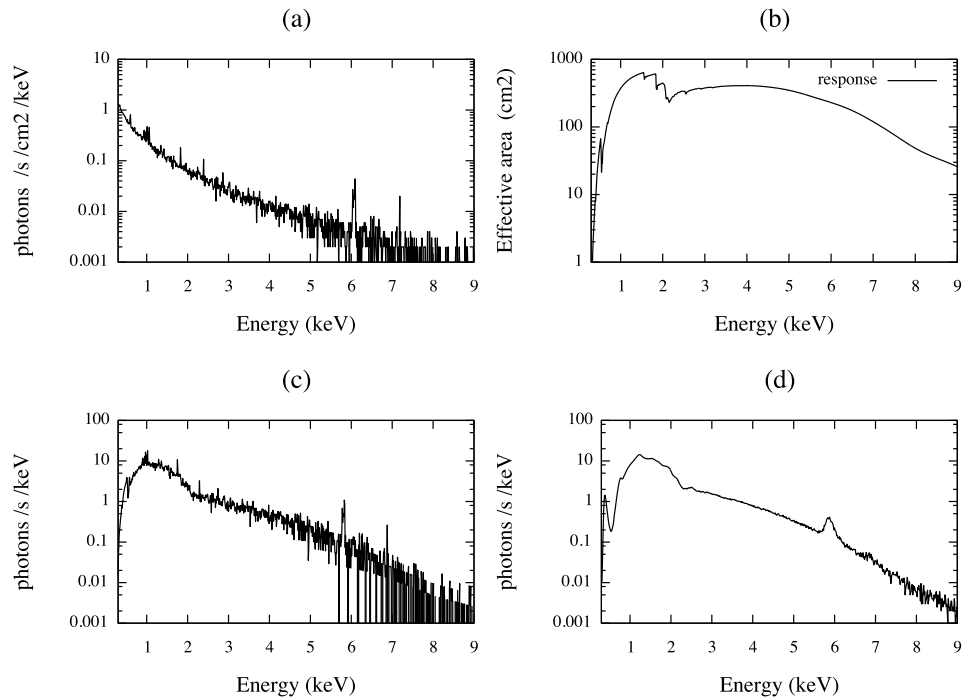


Figure 2.3: Effect of the detector response on the spectrum.

(a) The X-ray spectrum from the source as seen by a perfect detector (only including random noise). The exponential continuum and the emission lines are clearly visible.

(b) Detector efficiency (here pictured for *Chandra*'s ACIS-I spectrometer), in cm^2 .

(c) The spectrum in (a) after passing through a detector with the efficiency pictured in (b). The continuum is distorted (the effect is especially visible at low energy), but the lines are not affected.

(d) The observed spectrum: the continuum is deformed by the imperfect efficiency (*arf*) and the lines are smoothed by the limited resolution (*wrmf*).

2.3 THEORETICAL EMISSION MODEL

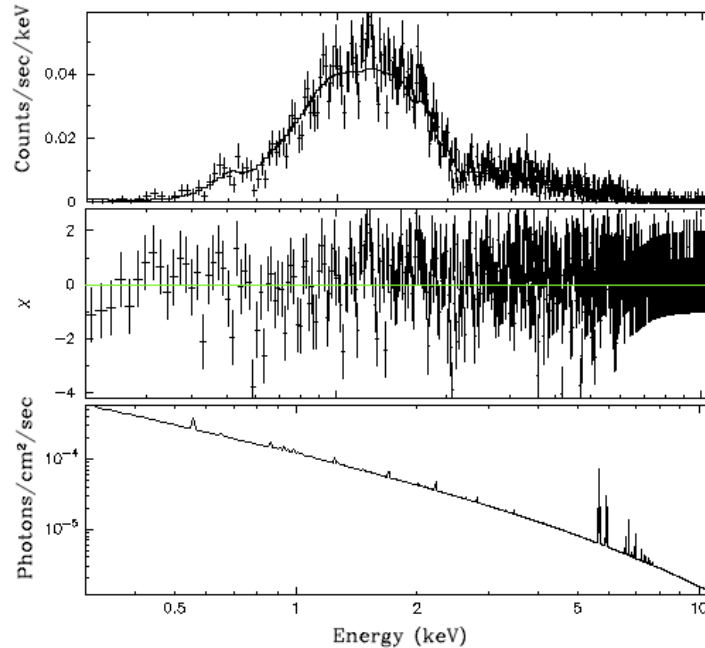


Figure 2.4: Observed X-ray spectrum of A1689 (*top panel*) fitted by the thermal emission model *mekal*. The fitting residuals are shown in the middle panel. The bottom panel shows the theoretical emission model, *mekal*, before convolution with the instrumental response.

X-rays spectra are useful in the sense that they provide us with information on the properties of the emitting gas. We can find the density and temperature of the intracluster medium by fitting a model to the X-ray spectrum. In general, spectral fitting is done in three steps:

1. Calculate a model spectrum, usually by numerical integration on a discrete grid (Fig. 2.4, bottom panel).
2. Multiply such spectrum by the response matrix of the instrument (a procedure known as ‘folding’ the spectrum).
3. Vary the model parameters (temperature, density, abundance...) to optimize the fit of the model spectrum to the data (Fig. 2.4, top panel).

2.3.1 MEKAL

The spectrum of a hot, diffuse gas can be described using the *mekal* emission code that is implemented in Xspec. The model is named after its creators Mewe,

Kaastra and Liedahl and has evolved from early work by Mewe and collaborators [37], starting from 1970 onwards. Today the code is one of the most widely used in spectral fitting and is a standard model incorporated in Xspec.

The code requires a number of parameter in order to calculate the X-ray spectrum: the most relevant for this work are the gas temperature and the normalization factor, that is just the emission integral $EI \equiv \int n_e^2 dV$, scaled by the distance to the cluster. The full expression of the normalization factor is

$$norm = \frac{10^{-14}}{4\pi[D_A(1+z)]^2} \int n_e^2 dV \quad (2.2)$$

where D_A is the angular distance and z the redshift. The factor of 4π in the normalization arises from the assumption that the emissivity is isotropic. The model also prompts for redshift and metallicity.

2.3.2 GALACTIC ABSORPTION

The X-ray spectrum from an extragalactic source does not reach our detectors unchanged. All radiation has to pass through the interstellar medium of our galaxy, where it is partly absorbed by the interstellar medium. The dominant mechanism is photoelectric absorption, called *wabs* in Xspec: when an X-ray interacts with an atom of the intergalactic medium, the photon completely disappears, transferring its energy to one of the electrons of the atom. The spectrum is consequently reduced by factor

$$M(E) = e^{-N_H \sum a_i \sigma_i(E)} \quad (2.3)$$

where a_i are the elements abundances and $\sigma_i(E)$ the absorption cross section of each element [39]. $N_H \equiv \int n_H dl$ is the hydrogen column density along the line of sight to the cluster. The Xspec implementation (called *wabs*) uses tabulated values for the cross section and metallicity [4, 39], and the only free parameter is the column density. I used the results from the weighted average of the LAB survey [28], that are accessible via the Nasa's n_H tool.

The resulting values are $n_H^{A1689} = 1.83 \times 10^{20} \text{ cm}^{-2}$ for A1689 and $n_H^{A2218} = 2.60 \times 10^{20} \text{ cm}^{-2}$ for A2218.

CHAPTER 3

Onion Peeling

RECOVERING THE 3D STRUCTURE of an observed quantity is a fundamental problem in astrophysics. In particular, the shape of galaxy clusters is quite an interesting property to know, not only because it determines the cluster's physics, but it also has an impact on the extraction of cosmological parameters [23], on the derivation of the cluster mass [31], and on the determination of the Hubble constant from a combination of X-ray and Sunyaev-Zel'dovich measurements [7].

A common method to say something on the 3D shape of a cluster relies on a combination of X-ray, strong and weak lensing data [31, 38]. In this thesis, I present a new method based on X-ray observations only. Using a single dataset has several advantages, for example, it's easier to control systematic errors. Additional information, or a useful comparison, comes from lensing and SZ data.

3.1 FROM 3D TO 2D...

Most astronomical objects can't be investigated directly due to their enormous distance, and the only thing we can see (if the detector resolution is good enough) is a two-dimensional image. The photon flux I through the detector window is the emissivity integrated along the line of sight. If Ω is the solid angle subtending the source,

$$I = \int_{\Omega} d\Omega \int \epsilon dl \quad (3.1)$$

and all the depth information has been lost during the projection from 3D to 2D.

Due to their fortunate properties, clusters of galaxies make a special case, and such information is not gone forever. The intracluster medium is so thin that all the emitted radiation leaves the cluster, so the observed spectrum is actually a mix of photons born at different depths. This transparency has a drawback though, because the signal from different regions mix up along the same line of sight, until it eventually hits the detector. It's our task to separate those photons which were born in the core from those who come from the outer region: they are still recognizable, in principle, if their temperature is different. This technique is known as deprojection.

3.2 ...AND BACK TO 3D

A geometrical technique to deproject the spectra was originally introduced by Gerard Kriss et al. in the early 80s, when the first spatially resolved X-ray data became available [30]. The method has been subsequently improved by many groups, including Buote, Ettori and Morandi [13, 19, 38] and, in the spherical case, has become a standard tool in X-ray cosmology.

The cluster is modeled as an onion-like structure, made up of concentric shells centered around the brightest point (Figure 3.1), which makes possible to find the true density and temperature in each shell by applying an iterative procedure. The outer shell is observed and analyzed first. Then, the next layer is analyzed, subtracting the signal from the outer shell, and so on until the core shell (think of peeling an onion). The deprojection can only be done by assuming a certain 3D shape of the cluster: the most common assumption, for simplicity or perhaps in lack of a better model, is spherical symmetry.

If we relax this assumption, the procedure can be extended to the more general case of a triaxial cluster. Then, assuming that the best shape will give the best fit to the data, we can use the deprojection algorithm as a tool to investigate the cluster shape. I will describe this method in details in Section 3.3 and following.

This method has the advantage of being fully non-parametric in the derivation of the profiles, although it still requires some assumptions on the shape, whether spherical or not. However, it requires good angular resolution, so we can bin the data in rings, and good photon statistics, because deprojected spectra are much more noisy than the observations.

There's another possible approach to the problem: instead of deprojecting the observed spectra, we could propose a theoretical model and compare it with real data. If we create a big sample of clusters with different shapes, we will eventually find the geometry that gives the best fit to the observations. I will discuss this approach in Chapter 4.

3.3 THE GEOMETRICAL DEPROJECTION

In this chapter I describe a general method for deprojecting images to reconstruct the 3D structure of the projected object. The starting point is the state of the art spherical algorithm, that I will adapt to the more general non-spherical case in Section ???. The method can be applied to X-ray or Sunyaev-Zel'dovich maps to determine the physics of the intracluster medium by recovering the 3D profiles of gas temperature and density [3]. Besides, it can provide a guess about the elongation of the cluster.

3.3.1 OBSERVING THE CLUSTER

We can think of a cluster as an onion-like structure, made up of thin concentric shells. Each shell is characterized by its own temperature and density, uniform within the cell volume, but different from shell to shell. In the non-spherical case, shells will be ellipsoids of varying axis ratio.

The image of the cluster is split in N two-dimensional rings (or annuli) of radius $r_1 < r_2 < \dots < r_N$. For each ring, we observe a spectrum, that we indicate

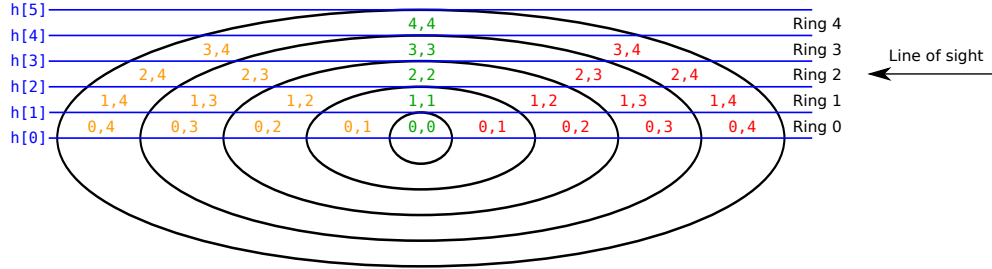


Figure 3.1: The overall structure. The lines labelled as *Ring 1*, *Ring 2*,... are lines of sight for an observer sitting off the right side of the page.

as S_i .

Let us define ϵ_j as the unitary signal radiated by the i -th 3D shell, in units of $keV cm^{-3} s^{-1}$. I choose the index convention such that the $i = 1$ goes to the innermost shell and N to the outermost. In the same way, the innermost observational ring has $j = 1$.

Now we need to project the emission along the line of sight. The contribution from the i -th shell to the brightness of the j -th ring is

$$S_{i,j} = \epsilon_i V_{i,j} \quad (3.2)$$

where $V_{i,j}$ is the fraction of the i -th shell that is subtended by the j -th projected ring. The nature of these volumes is purely geometrical, and their derivation is outlined in Chapter 3.5. Note that the volume matrix $V_{i,j}$ is triangular, with non-zero entries only for $i > j$.

The observed surface brightness I_j of the ring j is a weighted sum of contributions of all the inner shells:

$$\begin{aligned} S_1 &= \epsilon_1 \cdot V_{1,1} + \epsilon_2 \cdot V_{2,1} + \epsilon_3 \cdot V_{3,1} + \cdots + \epsilon_n \cdot V_{n,1} \\ S_2 &= \epsilon_2 \cdot V_{2,2} + \epsilon_3 \cdot V_{3,2} + \cdots + \epsilon_n \cdot V_{n,2} \\ &\vdots \\ S_n &= \epsilon_n \cdot V_{n,n} \end{aligned}$$

That generalizes to:

$$S_j = \sum_{i=j}^n s_{i,j} = \sum_{i=j}^n \epsilon_i \cdot V_{i,j} \quad (3.3)$$

The deprojection aims at inverting the set of equations above, i.e., recovering the values of ϵ_i from the observed projected signal S_j .

3.3.2 PEELING THE ONION

Assuming that we have subtracted the background correctly (which is not part of this thesis), from the spectrum of the n -th annulus we can easily recover the emissivity ϵ_n in the outer shell, as the sum in equation (3.3) consists of only one term $S_n = \epsilon_n V_{n,n}$. Temperature and density at radius r_n can be found by fitting the spectrum.

We can then proceed inwards and use the recovered emissivity ϵ_n to solve the equation for the adjacent ring, having index $n - 1$. Its brightness takes two contributions, from the n and the $n - 1$ shells,

$$S_{n-1} = \epsilon_{n-1} \cdot V_{n-1,n-1} + \epsilon_n \cdot V_{n,n-1}$$

which can be solved for ϵ_{n-1} .

This procedure is repeated from ring to ring until to the center of the cluster, finding the solutions in a recursive way. Finally, we can fit a theoretical model to each of the ϵ_n , to find temperature and density of the shell.

Given the iterative nature of this procedure, the errors associated to different radial annuli are not independent, because the uncertainty associated to each ring propagates to all the inner shells. For this reason, it is difficult to have a rigorous derivation of the uncertainties associated to the deprojected profiles. As a result, deprojected spectra are extremely noisy.

3.4 PLAYING WITH THE SHAPE

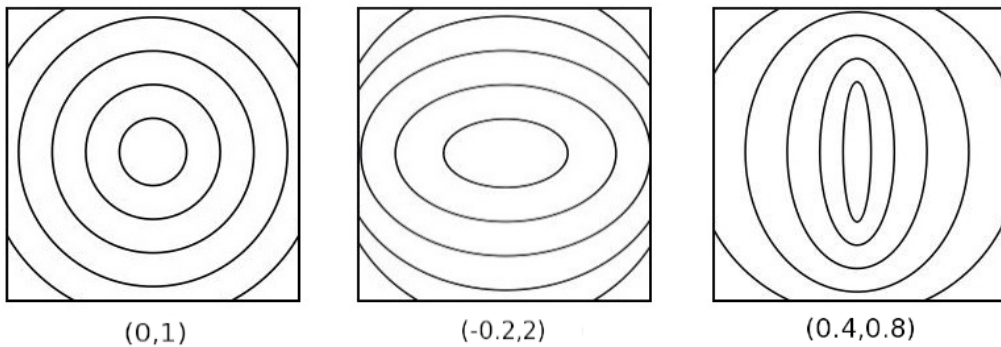


Figure 3.2: Examples of elliptical structures whose profile can be described by equation (3.5) and (3.6) for different choices of (α, β) . The structures are seen along the line of sight (going from left to right of the page), that is also the axis of symmetry. From left to right: a spherical cluster (*left*) followed by a cluster with a prolate core (*center*) and a cluster with an oblate core (*right*). The numbers in the brackets are the specific values of (α, β) chosen for each structure.

Let us start by giving a parametrization for a non spherical cluster. I use the onion-like structure introduced in Chapter 3.3, now allowing the shells to be ellipsoids. At this stage, I will be assuming axial symmetry, but the cluster ellipticity can vary as a function of radius. This is of course a simplified approach, but it seems justifiable as a first approximation. Studies of surface brightness maps in elliptical clusters confirms that they are well approximated by co-axial ellipsoids of similar axis ratio [29] and similar results are found in numerical simulations of cluster-size structures [18, 27].

A triaxial ellipsoid has an equation:

$$\frac{x^2}{a^2} + \frac{y^2}{b^2} + \frac{z^2}{c^2} = 1 \quad (3.4)$$

where a , b and c are the semi axes on the plane of the sky and line of sight, respectively. Because the clusters that I am going to analyze look circular in the sky, I assume axial symmetry and set $a = b = r$, where r is a radial coordinate.

For each shell, the dimensionless axis ratio

$$\xi_i = \frac{c_i}{a_i} \quad (3.5)$$

fully describes the shape of that layer. In general, the ratio will assume a different value for each layer –hence the indices in equation (3.5). In the simplest case, it evolves linearly with the radius

$$\xi(r) = \alpha \frac{r}{r_0} + \beta \quad (3.6)$$

that inserted in equation (3.6) reads

$$c = \left(\alpha \frac{r}{r_0} + \beta \right) r \quad (3.7)$$

where r_0 is a scale radius introduced to make the quantity α dimensionless, that we arbitrarily fix to $r_0 = 1$ Mpc.

The overall shape now depends upon the choice of (α, β) . The parameter β is a dimensionless quantity telling us what the cluster core looks like. If, for instance, $\beta = 1$, we have cluster with a spherical core, while we have a prolate core if $\beta > 1$. The cluster will look less and less spherical moving away from the central region due to the presence of the linear term αr . A positive choice of α makes the structure prolate at large radii, while a negative α gives an oblate structure.

Of course, not every choice of parameters is reasonable. The axis ratio must be bigger than zero and, although every positive value is ok for the sake of geometry, we expect real structures to have rather small ellipticities, as there is strong suggestion that most clusters are roundish or slightly elongated. A study

by Plionis et al. [41] on a sample of 6000 clusters reports that the observed projected ellipticity is $\langle e_{2D} \rangle = 0.6 \pm 0.2^1$, which has been converted into an intrinsic ellipticity of $\langle e_{3D} \rangle = 0.5 \pm 0.2$. In a study of 99 Abell clusters, De Theije et al [17] found that the distribution of ellipticities peaks around $e = 0.4$ with a maximum at $e = 0.8$. From their sample it is also shown shown that richer clusters are intrinsically more nearly spherical than the poorer ones. Rhee et al. found a [44] an ellipticity of $\langle e \rangle = 0.2 \pm 0.13$. Overall, we can conclude that the distribution of cluster shapes is found to be more consistent with a population of prolate clusters than with a purely oblate population [17, 29, 40].

Negative α of sufficiently large value will lead to the unphysical situation where outer layers become smaller than the inner layers. We can easily rule out this possibility by forcing the derivative of (3.14) to be positive for all radii of interest. For typical cluster scales $\sim 1\text{Mpc}$ the critical value of α is $\alpha_{crit} = -0.5$. I tested a range of ellipticities $\alpha \in [-0.5, 2]$, meaning that, for a roughly spherical core, the major-to-minor axis ratio in equation 3.5 goes from $-0.5 : 1$ of an oblate clusters to $3 : 1$ of a highly prolate one.

3.5 CELL VOLUMES

To successfully extend the deprojection to non-spherical structures, we need to calculate the volumes of all the cells. As mentioned in Section 3, we are interested in structures that are symmetric around the line of sight, which allows us to restrict to a two dimensional space, where we deal with simple ellipses of equation:

$$\frac{r^2}{R_i^2} + \frac{z^2}{c_i^2} = 1 \quad (3.8)$$

where r is a coordinate in the plane of observations, R_i and c_i are the semi-axis and z is the line-of-sight coordinate. The volume of a body of rotation around the z -axis, whose surface profile is enclosed by $f(z)$, is given by:

$$V = \pi \int_{z_{min}}^{z_{max}} (f(z))^2 dz \quad (3.9)$$

where f in this specific case is given by $f_i(z) = R_i \sqrt{1 - \frac{z^2}{c_i^2}}$, where i is the shell of interest.

The volume of the full ellipsoid can be found immediately by applying equation (3.9):

$$V = 2\pi \int_0^{c_i} R_i^2 \left(1 - \frac{z^2}{c_i^2}\right) dz = 2\pi R_i^2 \left[z - \frac{z^3}{3c_i^2} \right]_0^{c_i} = \frac{4}{3} R_i^2 c_i$$

¹The ellipticity is defined as $e = 1 - \frac{\Lambda_2}{\Lambda_1}$, Λ_1 and Λ_2 being the major and minor semi-axis, respectively.

where the extra factor 2 accounts for the half-ellipsoid in the semi-plane $z < 0$.

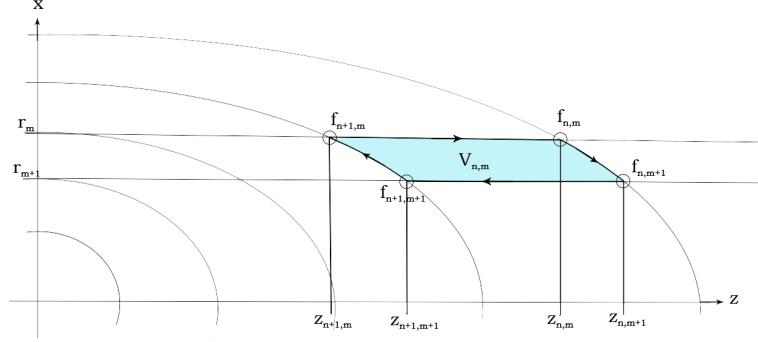


Figure 3.3: The volume of a single cell can be found integrating around the edge of the cell projection in the x,z -plane and multiplying by 2π .

Let's consider now the 2-dimensional cross-section of a single cell (Figure 3.3) The boundaries of the cell are made up by four elements: the outer shell; the inner shell; and the upper and lower straight lines marking the annuli j and $j - 1$. The corner points of the shell on the outer ellipse will be named $f_{i,j}$ and $f_{i,j-1}$, whereas the matching point on the inner ellipse are named $f_{i-1,j}$ and $f_{i-1,j-1}$.

We can find the volume of the cell by integrating along the borders of the cells following the arrows in Figure 3.3, so that the inner part is subtracted from the outer part

$$\frac{V(i,j)}{2\pi} = \int_{z_{i-1,j}}^{z_{i,j}} R_j^2 dz + \int_{z_{i,j}}^{z_{i,j-1}} (f_i(z))^2 dz - \int_{z_{i-1,j-1}}^{z_{i,j-1}} R_{j-1}^2 dz - \int_{z_{i-1,j-1}}^{z_{i-1,j}} (f_{i-1}(z))^2 dz$$

The values of z in the corner points are marked as $z_{i,j}$. This points lie at the intersection between the i -th shell and the $r = r_j$ line.

$$\begin{cases} \frac{r^2}{R_i^2} + \frac{z^2}{c_i^2} = 1 \\ r = R_j \end{cases} \quad (3.10)$$

and their general expression is $z_{i,j} = c_i \sqrt{1 - \left(\frac{R_j}{R_i}\right)^2}$

The last thing we need to know before evaluating the integral is how the ellipse semi-axes c_i scale with the radius. It's reasonable to assume a linear relation as those described in Chapter ??, so that $c_i = R_i \cdot (\alpha \cdot R_i + \beta)$.

This expression allows us to integrate numerically around the borders and evaluate the volumes of all individual cells in the cluster.

3.6 MODELING THE INTRACLUSTER MEDIUM

The shape of the cluster can be measured only if there is a temperature gradient between the core of the cluster and its outskirts. If the cluster was isothermal, the signal from every volume of gas would have the same $e^{-E/T}$ exponential tail. Integrating along the line of sight would still yield a $\sim e^{-E/T}$ profile, regardless of the inner structure.

Fortunately, observations tell us that most clusters are not isothermal, just like they are not perfectly spherical: at large radii, the temperature falls off with a power-law profile [45, 49]. Things are more complicated in the center of the cluster, where the presence of cooling flows might affect the temperature, producing a cusp or a flat core [49].

In the next few sections I will gradually construct an analytical expression for the gas temperature and density, that can adequately describe a wide range clusters' profiles. I start from a simple toy model (Section 3.7), that I can use as testing ground, and then include more complicated features (Section 3.8 and 3.9). I will apply the technique to galaxy clusters A1689 in Section 3.10.

3.6.1 HOW TO FAKE A CLUSTER

Xspec allows the user to simulate observations of an X-ray source through the *fakeit* command. These 'fake' data can be extremely realistic, as they are tailored to mimic data from a specific telescope by folding with relevant response files. Throughout this work, I simulate mock *Chandra* data.

For each observational ring, the spectrum can be adequately described by a combination of *mekal* models weighted according to our results in Chapter 3.3. In Xspec language, we expect the flux through the ring j to be

$$S_j = A_j \cdot wabs(N_H) \sum_{i=j}^n mekal(T_i, n_{e,i}) \cdot V_{i,j}(\alpha, \beta) \quad (3.11)$$

where A_j is the area of the ring. Let's have a closer look at equation (3.11):

1. To begin, a *mekal* model is used to find the emission from a unitary cell of plasma. The code estimates the cooling function for a gas of temperature T , with normalization proportional to the electron density n_e^2 . Other required parameters are the cluster's redshift and abundance.
2. Then I make a weighted sum the shells of interest. The factors V_{ij} simply scale the emission to the volume of the emitting cell.
3. Finally, the *wabs* component corrects for galactic absorption. Its strength depends on the hydrogen column density N_H .

The spectrum is integrated over some exposure time and there's an option to add random noise.

For testing purposes, I set all the numbers to their value in galaxy cluster A1689 (see Chapter 3.10).

3.7 A TOY MODEL

3.7.1 TEMPERATURE PROFILE

Because the projection effect arises from a temperature gradient, I want, as a first step, to use a simple profile that makes this difference as pronounced as possible. Observations suggest that the temperature decay in the outer region follows a power-law (Fig. 3.7),

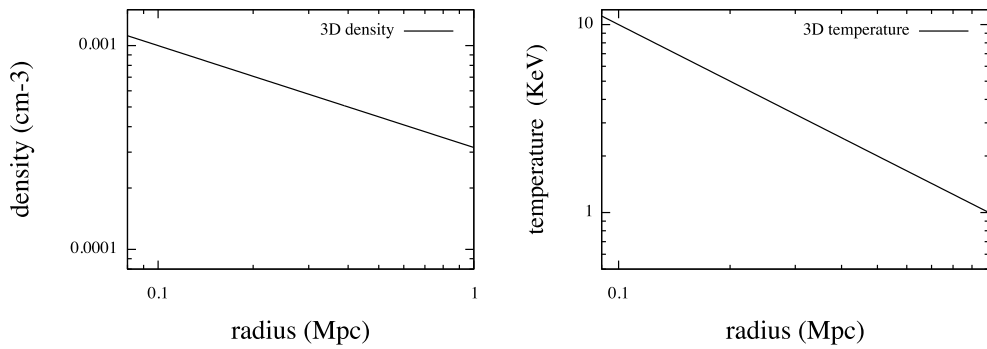


Figure 3.4: *Left:* the simplest density profile is a single power law (3.12). On the x -axis is a radial coordinate for a typical cluster size of 1Mpc. *Right:* single power law temperature profile (3.13).

$$T(r) = T_0 \left(\frac{r}{r_0} \right)^{-a} \quad (3.12)$$

where T_0 is a normalization and has units of keV and r_T is a characteristic length [49]. I choose a moderate negative slope ($a = 1$) and model a cluster that emits in the soft X-rays range². All the parameters are listed in Table 3.4.

²X-rays from 0.12 to 12 keV are conventionally referred to as ‘soft’, while more energetic X-rays, namely 12 to 120 keV is referred to as ‘hard’. The distinction comes from their penetrating abilities. Clusters of galaxies are known to emit soft radiation [45].

3.7.2 DENSITY PROFILE

The electron density determines the normalization of the spectrum, that is proportional to n_e^2 , but does not affect its shape. If the gas density profile is flat, or not very steep, each region will contribute more or less with the same amount of X-rays. In a real cluster, however, the density falls quickly from 10^{-3} cm^{-3} in the core to 10^{-5} cm^{-3} in the outskirts [45], causing each shell to radiate less energy than the previous one, until we cannot detect anything at all in the outermost region. This also means that the contribute from the outer shells will be smaller (a few percent of the total [19]) and difficult to measure. The problem can be partly mitigated by choosing larger radial bins in the outer region, but it remains one of the biggest observational limits to this kind of technique.

I start by assuming, for testing purposes only, a power law decay (Fig. 3.4)

$$n_e(r) = n_0 \left(\frac{r}{r_0} \right)^{-b} \quad (3.13)$$

with a moderate slope of $b = 0.5$, which is less steep than what is found for most clusters. Again, n_0 is the normalization and r_0 is a scale radius.

	T_0	r_0	n_0	a	b	α_{vol}	β_{vol}
toy model	(keV)	(Mpc)	10^{-3} cm^{-3}	(Mpc)			
	10	0.1	10	1	0.5	0.5	1

Table 3.1: Toy model parameters from in section 3.7.

3.7.3 RESULTS

With these profiles, I construct a slightly prolate cluster with a roundish core. Using the notation introduced in Chapter 3.4, the cluster's z -axis, which lies along the line of sight, is parametrized as

$$z = (\alpha r + \beta) r \quad (3.14)$$

with $(\alpha, \beta) = (0.5, 1)$. The structure is about 1 Mpc in size.

This model cluster can be used as a testing ground for the shape-finding algorithm. The final goal is to retrieve the correct value of (α, β) , but I also want to reconstruct the 3D temperature and density profiles.

I divide the structure in $n = 10$ equally spaced annuli that are 100 kpc wide, and simulate the emission from each of them by using equation (3.11). Then I test a range of ellipticities by looping through different values of α . For each

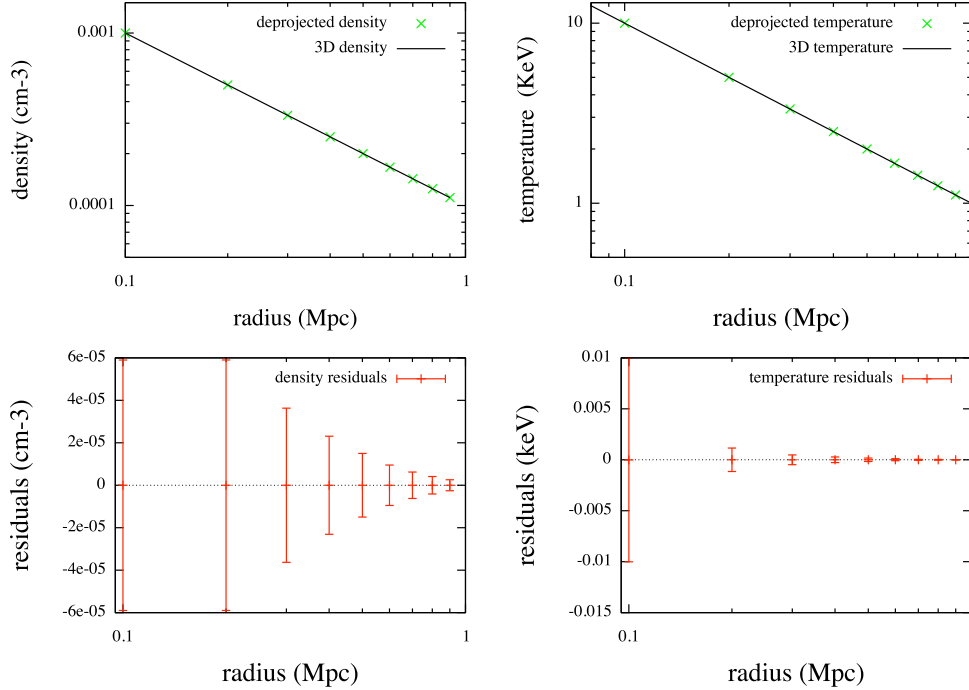


Figure 3.5: *Top panel:* model density profile and best-fit deprojected density profile (*left*) in units of 10^{-3}cm^{-3} . *Right:* same for the model temperature profile and deprojected temperature. Errorbars are too small to be plotted.

Bottom left: residual plot for density. *Right:* temperature profile with errorbars from Xspec. The residuals are close to zero, have small errorbars and generally indicate a good fit.

step, I calculate a new set of volumes that are used to peel the spectra in the way outlined in Section 3.3. The deprojection returns n clean spectra, which can be fitted to a *mekal* model with density, temperature and normalization as free parameters. All the mathematical operations between spectra, like subtraction of the outer layers, are handled via the *mathpha* software from the Nasa’s Ftool package [20]. The best fit results, with errorbars, are shown in Figure 3.5. From Figure 3.6 we can see that the deprojected profiles fall almost exactly on top of the theoretical model. The errorbars are so small that they can’t be seen in this plot, but a residuals plot reveals that residuals are regularly arranged around zero. Inner rings have much bigger errorbars, which does not come unexpected as the deprojection is an iterative procedure, and therefore we expect the errors to be correlated.

For each step I also record the χ^2 value as function of α , when all the other variables are maximized over (Fig. 3.6). In this simple model the χ^2 distribution is extremely sensitive to variations in the shape, and a deep minimum can be

found corresponding to the true value $\alpha = 0.5$. The value of α minimizing χ^2 is the same that maximizes the likelihood function

$$\mathcal{L}_\alpha = e^{-\frac{\chi_\alpha^2}{2}} \quad (3.15)$$

For a one-dimensional χ^2 (like this), a standard error of 1σ corresponds to a contour of

$$\chi = \chi_{min}^2 + 1 \quad (3.16)$$

or $\ln \mathcal{L} = \ln \mathcal{L}_{max} - 1/2$ (Fig. 3.11a). Thus, the final estimate of the cluster ellipticity is $\alpha = 0.5^{+0.14}_{-0.11}$. The probability curve is not symmetrical, hence the different upper and lower limits.

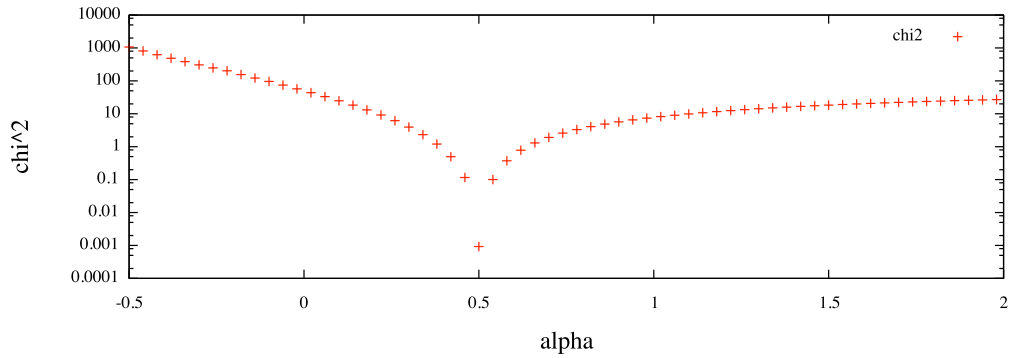


Figure 3.6: One dimensional χ^2 for different values of α , when the other variables are maximized over. The sharp minimum around $\alpha = 0.5^{+0.14}_{-0.11}$ reveals that we are dealing with a prolate cluster, as expected.

3.8 β -MODEL

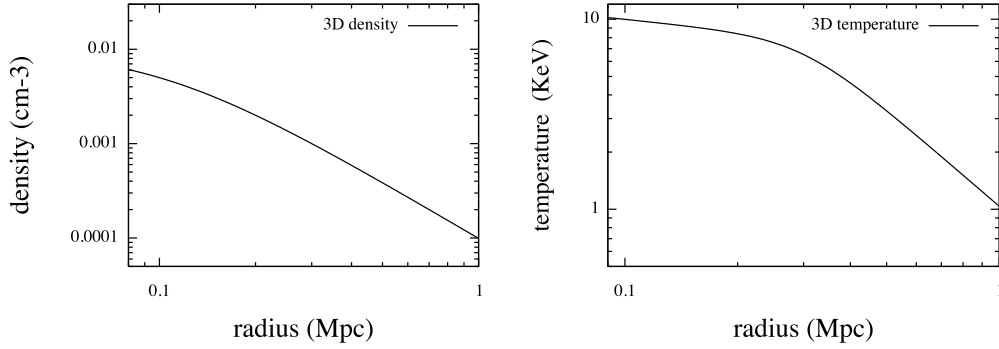


Figure 3.7: β -model density profile (*left*) and double power law temperature profile (*right*).

Now I want to set up a realistic profile for the cluster density. A simple profile to describe the distribution of gas in a relaxed cluster in hydrostatic equilibrium is the β -model [14]:

$$n(r) = n_0 \left(1 + \left(\frac{r}{r_c} \right)^2 \right)^{-\frac{3\beta}{2}} \quad (3.17)$$

where, again, n_0 is central number density, r_c is a core radius, within which the density is relatively flat. The parameter β is $\sim 2/3$.

This model has the big advantage of keeping the number of parameters to a minimum, while still providing a decent fit, and has been extensively used to fit X-ray luminosity profile. However, it has some limits, especially in describing the central region [49]. A more general profile that accurately describes the actual features of clusters will be introduced in the next section.

	T_0	r_T	a	b	c	n_0	r_n	β	α_{vol}	β_{vol}
β -model	(keV)	(Mpc)				(cm^{-3})	(Mpc)		(Mpc^{-1})	
	10	0.5	0.2	5	1.5	0.1	0.1	0.6	0.5	1

Table 3.2: Model parameters, section 3.8.

The temperature profile can also be improved. The X-ray brightness profiles are often found to steepen at large radii [49]. This change in slope can be

described by a double power law

$$t(r) = T_0 \frac{(r/r_t)^{-a}}{\left(1 + \left(\frac{r}{r_t}\right)^b\right)^{\frac{c}{b}}} \quad (3.18)$$

which has a slope of $-a$ at small radii and slope of $-c - a$ at large radii. The transition occurs near the radius r_t , and has a width controlled by the parameter b .

The deprojected quantities (Fig. 3.8) correctly reproduce the model profile. The χ^2 still has a deep minimum around $\alpha_{min} = 0.5^{+0.31}_{-0.25}$, that is, however, not as narrow as the one found in the testing phase (for a comparison, see Fig. 3.6). This seems reasonable, since the density profile is steeper (now spanning two orders of magnitude), that makes it difficult to correctly weight the emission from the outer layers.

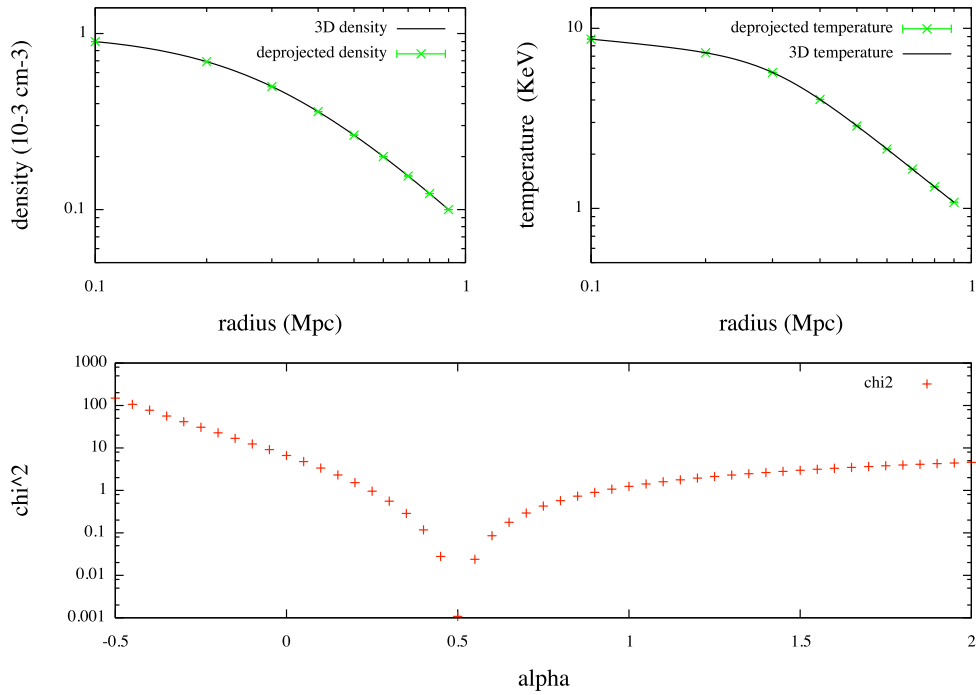


Figure 3.8: *Top panel:* model density profile and best-fit deprojected density profile (left) in units of cm^{-3} . *Right:* same for the model temperature profile and deprojected temperature. In this plot, as in Fig. 3.6, the errorbars are too small to be seen.

Bottom: χ^2 as a function of the shape parameter α . The trend here is similar to the one in Figure 3.6 and a minimum can be found for $\alpha_{min} = 0.5^{+0.33}_{-0.21}$.

3.9 COOL CORE CLUSTERS

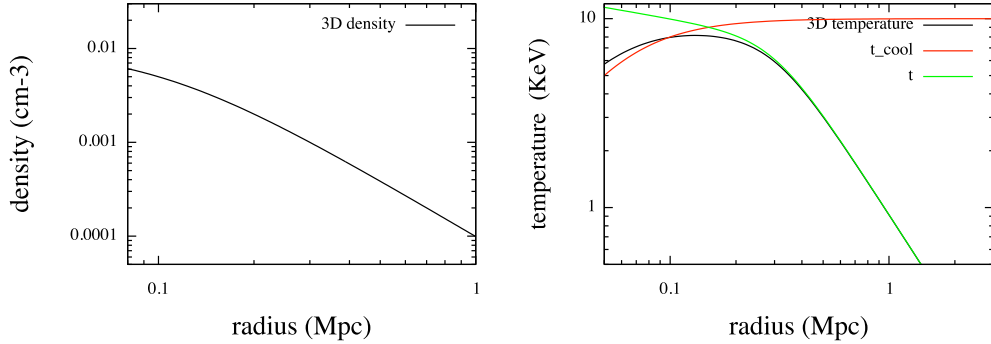


Figure 3.9: *Left:* density profile in a cool core cluster. *Right:* temperature profile (black), showing the contribution from cooling flows in the cluster core (red) and the broken power-law profile at large radii (green).

There are at least two classes of galaxy clusters. Clusters with a dense core show a temperature decline in the central region, suggested to be the results of radiative cooling flows [49, 50]. Around the cooling radius $r_{cool} = 0.1 \div 0.2 r_{200}$ there's a broad peak, after which the temperature decreases steadily. In clusters with moderate central densities (typically below $10^{-2} cm^{-3}$) the temperature profile towards the center is flat or slightly increasing. These clusters are known as non cool-cored.

Vikhlinin et al. [49] suggested that the temperature decline in a cool core cluster could be empirically described by an additional term,

$$t_{cool}(r) = \frac{x + T_{min}/T_0}{x + 1} \quad (3.19)$$

with

$$x = \left(\frac{r}{r_{cool}} \right)^{a_{cool}} \quad (3.20)$$

where a_{cool} is the temperature slope in the core and $\frac{T_{min}}{T_0}$ quantifies the magnitude of the decrement [49]. Outside the cooling region, the temperature profiles of most clusters are self-similar (if they are scaled to the same overdensity radius) and are well described by equation 3.18.

The final model for the three-dimensional temperature profile is the product of equations (3.19) and (3.18)

$$T_{3D}(r) = t_{cool}(r) t(r) \quad (3.21)$$

This model has eight free parameters, and can describe most kinds of smooth temperature distributions. In the same way, the gas density in the center of

relaxed clusters can be cusped, too [49]. We can modify the flat core in the traditional β -model [49]:

$$\frac{n_0}{\left(1 + \frac{r^2}{r_c^2}\right)^{\frac{3\beta}{2}}} \rightarrow n_0 \frac{\left(\frac{r}{r_c}\right)^{-\gamma}}{\left(1 + \left(\frac{r}{r_c}\right)^2\right)^{\frac{3\beta}{2} - \frac{\gamma}{2}}} \quad (3.22)$$

I also bin the observations in a different way, taking smaller annuli that are $\sim 50kpc$ wide close to the center, and larger bins in the outer part, where the X-ray luminosity is lower. We would expect the temperature cusp to interfere with the possibility of detecting the shape thanks to the changes in the X-ray temperature. If the profile is peaked, indeed, some regions of gas in the inner part would be at the same temperature as some other region far away in the outer part. If this is true, the photons coming from different region are no longer distinguishable.

As shown in figure 3.10, the effect is still detectable, although the χ^2 is considerably flattened and the errorbars are much bigger than in the previous case. The χ^2 has a minimum centered around $\alpha_{min} = 0.5^{+1.23}_{-0.38}$ but the uncertainty on the value is so big that covers most of the allowed parameter space. However, the results favor prolate structures ($\alpha > 0$) rather than oblate ($\alpha < 0$).

A comparison in the determination of α in the three clusters examined so far is shown in Figure 3.11.

3.9.1 WHAT WE LEARNED FROM THE SIMULATIONS

Overall, during this testing phase all the three-dimensional profiles were recovered with good precision (at worst a few percents) and the residual analysis shows that the method does not suffer from any intrinsic bias. The shape of the cluster cannot be constrained with the same precision, especially in the case of more complicated, cusped profiles; but the effect, albeit small, is always detectable. The results are good enough to discriminate between prolate and oblate structures. In the next Chapter, I will try to apply the same procedure to a real cluster: A1689.

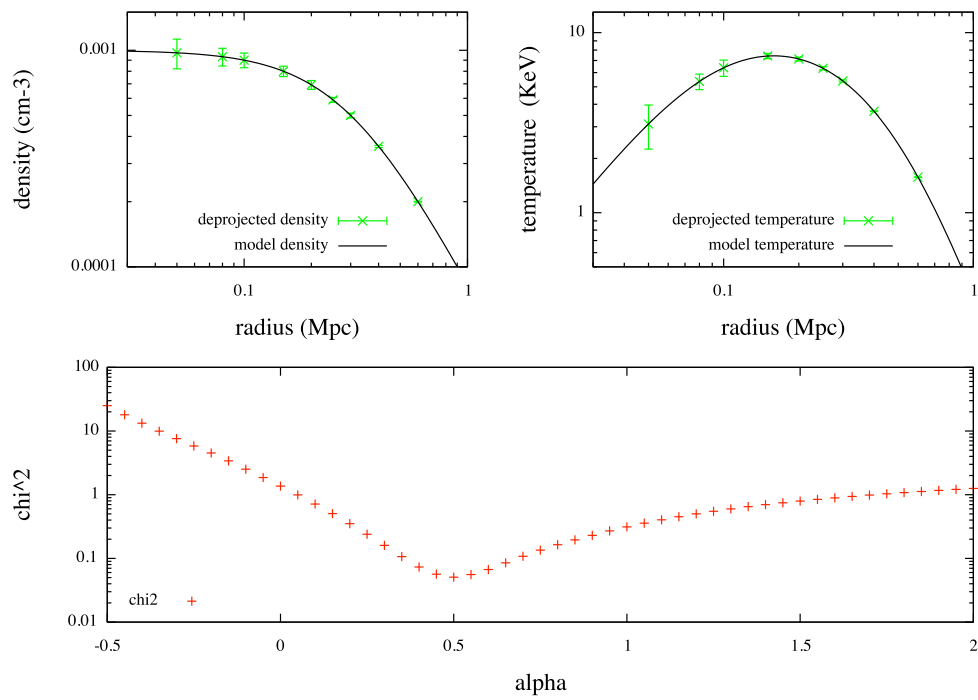
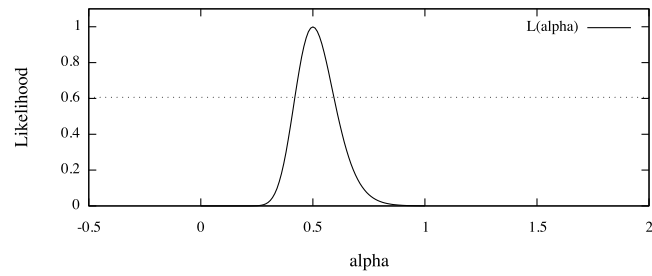
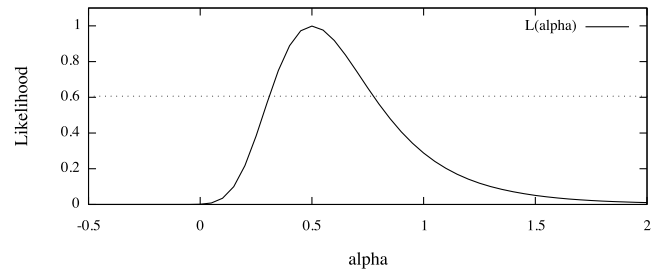
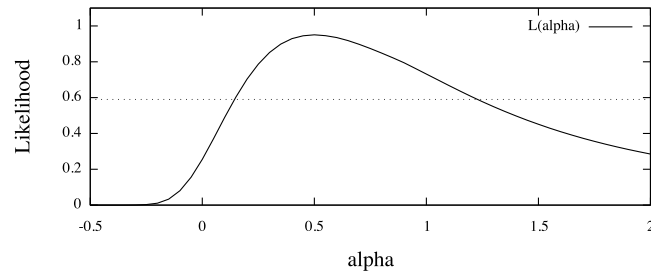


Figure 3.10: *Top left:* best-fit deprojected density profile (*left*) in units of cm^{-3} . *Top right:* deprojected temperature profile, in keV . The underlying theoretical model is plotted in solid black.

Bottom: $\chi^2(\alpha)$ distribution when all the other parameters have been maximized. Although considerably flatter, a minimum for $\alpha_{min} = 0.5^{+0.72}_{-0.29}$ can still be found.



(a) Toy model

(b) β -model

(c) Cool core cluster

Figure 3.11: The likelihood function \mathcal{L} (equation (3.15)) for the three structures analyzed in this chapter. The one-dimensional contour $\mathcal{L} = \ln \mathcal{L}_{max} - 1/2$ used to find the 1σ error is shown as a dotted line. All the curves are peaked around the cluster's true value $\alpha = 0.5$. However, the sharp peak in (a) is progressively broadened when adding more complicated features to the cluster profile. It's worth noticing that the probability curves are not symmetrical, with positive α -values being more likely than negative α -values. This is a good indicator of a prolate structure.

Toy model	T_0 (keV)	a						
	10	1						
Double power-law	T_0 (keV)	r_T (Mpc)	a	b	c			
	7	0.3	0.2	5	1.5			
Cool core Cluster	T_0 (keV)	r_T (Mpc)	T_{min} (keV)	r_{cool} (Mpc)	a	b	c	a_{cool}
	7	0.3		0.05	0.2	4	0.4	2

Table 3.3: Temperature parameters, summary.

Toy model	n_0 (cm^{-3})	b	α_{vol}	β_{vol}		
	10	1	0.5	1		
β -model	n_0 (cm^{-3})	r_c	β	α_{vol}	β_{vol}	
	1	0.3	0.6	0.5	1	
Cool core cluster	n_0 (keV)	r_c (Mpc)	β	γ	α_{vol}	β_{vol}
	10	0.3	0.6	0	1	1

Table 3.4: Density and shape parameters, summary.

3.10 ABELL 1689

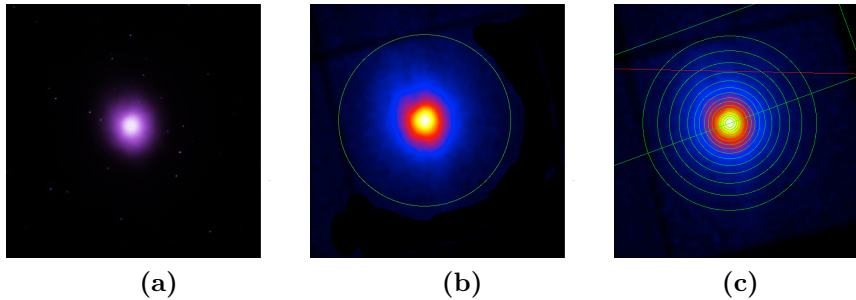


Figure 3.12: (a) *Chandra* image of Abell 1689 showing the logarithmic number of counts in the X-ray band. (b) X-ray morphology of the cluster [43]. (c) The radial binning (in green) that has been used for the deprojection [43].

A1689 is a massive cluster at moderate redshift ($z = 0.183$) that has been extensively observed in the X-ray band. The cluster has regular X-ray contours (Fig. 3.12b), whose projected ellipticity is as small as $\epsilon \simeq 0.08$ [53]. This would be taken as an indicator of a relaxed, nearly spherical structure, if big discrepancies between strong lensing masses and masses from X-rays didn't bring up the idea that A1689 may in fact be an elliptical structure, that is conveniently aligned with the line of sight [31, 38]. Thanks to its properties (symmetry along the line of sight; suspected non-sphericity), A1689 makes an optimal candidate to test the deprojection.

I use the full two-dimensional spectrum from a long observation that was conducted with *Chandra*'s spectrometer ACIS-I in March 2006. The background has been subtracted from the data and the point sources removed. The data are binned in 12 circular annuli centered around the X-ray peak. The size of the annuli, visible in Fig. 3.12c, was chosen in a way that the number of counts in each ring was comparable. The metallicity is set to 0.37 and the redshift to $z = 0.183$, the values reported in the *Heasarc* catalog [1]. Using Xspec to fit the observations confirms a redshift of $z = 0.177 \pm 0.009$ and a metallicity $Z = 0.48 \pm 0.08$.

3.10.1 PEELING THE CLUSTER

Just as done in the previous Chapters, I peel the cluster's layers, starting from the outer ring and proceeding towards the center. To each deprojected layer I fit a *mekal* model to find the temperature and the density of the gas. This procedure is repeated for different geometries by spanning a range of α and β , trying to find the shape that gives the best fit. The best-fit results are shown in Figure 3.14.

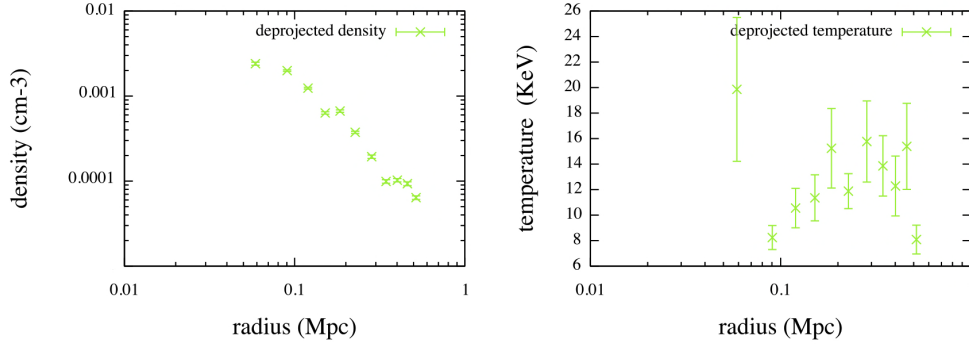


Figure 3.13: Results of the deprojection of A1689. *Left:* best fit density profile, with errorbars. *Right:* best fit temperature profile, with errorbars.

The density is relatively easy to constrain, because it comes from the normalization of the spectrum. The best-fit profile, shown in Figure 3.13, falls in the correct range 10^{-3} to 10^{-5} cm^{-3} and has errorbars of the order of a only few percent.

The temperature profile (Fig. 3.13), on the other hand, is irregular and affected by big uncertainties, but overall suggests a cool core cluster. The deprojected temperatures are slightly higher than average cluster temperatures, but their values seem in agreement with the global temperature of A1689, that is $T = 10.5 \pm 0.1 \text{keV}$ (from spectral fitting with Xspec). The temperature spike in the inner ring seems compatible with the presence of a central black hole [26], whose gravitational field would compress the inflowing gas, thus causing the temperature peak. In this sense, the peak could be used as a black hole diagnostic. However, detections of central temperature peaks in galaxies are rare [25] and this hypothesis has, therefore, yet to be verified observationally. In part this reflects the difficulty in obtaining precise temperature measurements on scales of a few hundred parsecs.

Overall, the biggest difficulty is that the deprojected spectra are so noisy that it's difficult to have a good handling of the spectrum exponential cut-off, which is crucial to determine the temperature. The problem is especially visible for the inner rings, which undergo a higher number of iterations. Figure 3.15 shows the emission of the innermost ring before and after the deprojection: the number of counts in the final spectrum (Fig. 3.15b) is merely reduced by a factor two, but the noise has increased so much that most of the features got lost. The fit χ^2 (Fig. 3.14) is almost flat, with a slight preference for prolate geometries. It was not possible to find any minimum.

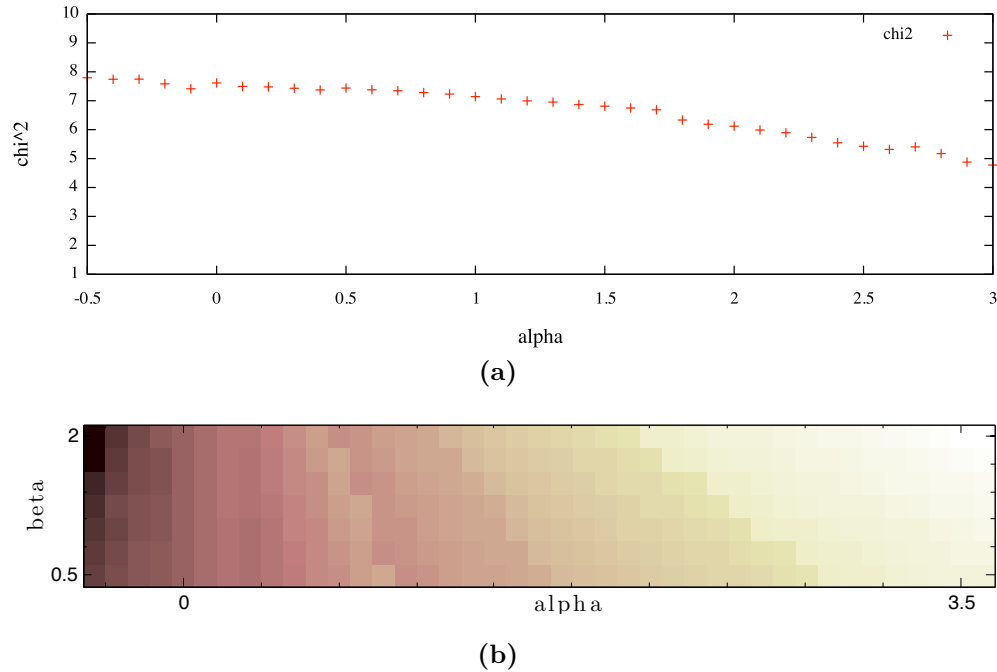


Figure 3.14: (a) The χ^2 profile is almost constant and, although it shows a slight preference for positive high values of α , it is not possible to constrain the shape. A longer run until $\alpha = 10$ still was not able to find a minimum. (c) The χ^2 profile is almost constant and, although it shows a slight preference for positive high values of α , it is not possible to constrain the shape. A longer run until $\alpha = 10$ still was not able to find a minimum. (b) χ^2 map if both α and β are allowed to vary. Light regions are for low values of χ^2 , dark regions are for higher χ^2 . There's a preference for prolate geometries ($\alpha > 0$, $\beta > 1$), although the differences are minimal.

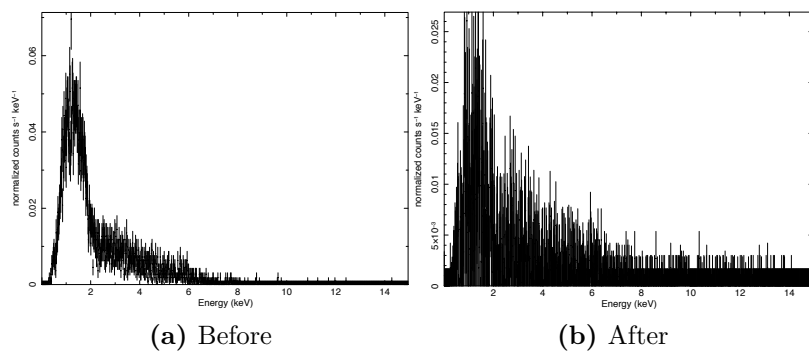


Figure 3.15: Observed spectrum of the innermost ring $n = 1$ (a) and the same spectrum when the outer layers have been peeled off (b).

The same procedure has been applied to Abell 2218, obtaining similar results (see Appendix A). For both clusters, the shape could not be constrained. Overall, the results suggest that variations in the X-ray spectrum induced by the cluster shape are extremely small and hard to detect, unless the quality of the observations is excellent. Deprojecting the cluster can only make the problem worse, because the signal to noise is further reduced at every iteration. It is possible that rebinning the spectra might slightly improve the results but, with the current data, this method is just not sensitive enough.

In the next chapter, I will try to solve the problem from a different perspective.

CHAPTER 4

A Monte Carlo approach

IN THE PREVIOUS CHAPTER I used the observations as a starting point, and tried to work the way back to the theoretical model. Now I'm going to follow a different approach: starting from a theoretical model, I will adjust the parameters to reach the best fit with the observations. Because the model is defined in a three-dimensional space whereas observations are only two-dimensional, I still need to make a projection to compare the quantities.

The idea is simple, the only requirement being that we can quickly generate a large number of clusters with the desired properties. We also need an efficient tool to explore the parameter space, like a Monte Carlo sampler.

In contrast to the deprojection, which was non-parametric, this method requires that we make some assumptions about the specific structure of the cluster: in particular, we need to set up an expression for the cluster temperature, density and geometry. Then we calculate the X-ray emission from a wide range of clusters with different profiles. We are of course interested in finding the set of parameters that gives the best resemblance of the theoretical spectrum to the the observations.

4.1 MONTE CARLO METHODS

The expression Monte Carlo (MC) indicates a family of probabilistic methods that can be successfully employed to solve complex problems, such as fitting problems in high-dimensional spaces. The technique makes use of random numbers to draw samples from a large system, with the idea that, if the samples are chosen in a smart way, they will be representative of the system as a whole. The great advantage of the MC methods is that it is possible to include many parameters for a relatively small computational time.

The sampler jumps around in the parameter space, taking random steps governed by a probability function. If the next point has higher probability than the current position, the step is taken. If the next step is to a point of lower probability, the step can still be accepted, with probability $P(new)/P(old)$. This way of jumping around is known as 'Markov chain', and describes a random walk where the probability distribution at each step only depends on the present position (but not on the specific way you got there¹). Since successive steps are correlated, the Markov chain may need to run for a considerable time to generate samples that are effectively independent (Fig. 4.4).

4.1.1 METROPOLIS ALGORITHM

This idea expressed above was formalized in the 50s by Metropolis and coworkers [36], who were trying to describe how a thermodynamic system finds the lowest

¹Also known as the drunkard's walk.

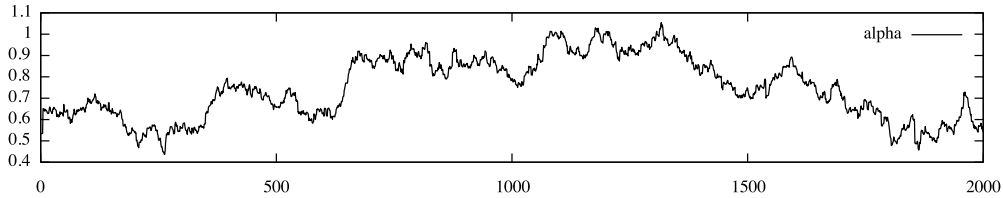


Figure 4.1: Time evolution of one of the variables (α) during 2000 iterations of the MCMC. This chain is made by highly correlated samples, and has to be ‘thinned’ by a factor large enough that the chain has time to move to an independent configuration.

energy state. If the system is in equilibrium at temperature T , each configuration has a probability proportional to the Boltzmann factor,

$$p(E) \sim e^{-E/kT} \quad (4.1)$$

where k is the Boltzmann constant. The key contribution of the Metropolis paper was the idea that the system will only change its configuration from a state of energy E_i to E_{i+1} with probability

$$p(E) = \begin{cases} 1 & \text{if } E_i < E_{i+1} \\ e^{-(E_2-E_1)/kT} & \text{if } E_i > E_{i+1} \end{cases} \quad (4.2)$$

Most of the time, the system will be jumping downhill, towards configurations of lower energy. Nevertheless, there’s a small chance of the system occasionally choosing to jump uphill, to ensure that we don’t get trapped in a local minimum. The lower the temperature, the less likely is any significant uphill excursion.

The Metropolis algorithm can also be used to minimize functions for other than thermodynamic system: all that is required is a function for calculating the probability given a set of parameter values. To search for a minimum in the parameter space, the energy can be replaced by a χ^2 estimate.

4.2 COSMOMC

CosmoMC is a Monte Carlo engine for exploring cosmological parameter space. The code was originally written to do theoretical power spectrum calculations with CAMB [32], but it can also be compiled as a generic sampler. The package is available online [33] and contains two programs: the first, *cosmomc*, does the actual Monte Carlo, while the second program, *getdist*, does importance sampling and statistical analysis of the chain.

In the next paragraphs I will describe some parts of the MC that require special attention.

4.2.1 BURN IN

The Markov chain starts from a point that is set by the user, and then the algorithm runs for several steps until the initial state is forgotten. These samples, which are discarded, are known as ‘burn-in’. After this transient, the chain approaches a stationary distribution (Fig. 4.4) where the set of accepted values represents a sample from the probability distribution $p(x)$.

4.2.2 PROPOSAL DISTRIBUTION

At each step, a new (tentative) state is generated by the proposal density. The algorithm works better if the proposal density is similar to the target distribution, $p(x)$, whose shape is unfortunately unknown. This problem can be overcome by running a test chain with a simple proposal (such as a n -dimensional gaussian) in order to estimate the covariance matrix. The matrix contains informations about how the parameters are correlated, and can be used as an input for a more realistic proposal to be used in the next runs.

4.2.3 STEP SIZE AND ACCEPTANCE RATE

The proposal length scale (which determines the step size) is usually chosen to be short relatively to the size of the system. The reason for a small length scale is that, for most high-dimensional problems, a large step from a point is very likely to end in a state that has very low probability, and such steps are unlikely to be accepted. The disadvantage of taking small steps, on the other hand, is that they will result in a random walk through highly correlated samples, which takes a long time to get anywhere. The fraction of proposed samples that is accepted is known as ‘acceptance rate’. In the steps are too small, the acceptance rate will be high, but the chain will mix slowly and take a long time to converge. The desired acceptance rate depends on the target distribution, but it has been shown that the ideal acceptance for a single gaussian is 50% [51]. For more complicated distributions, the step size of each parameter should be tuned by trials and errors. I found acceptable results with a rate of 60%, although a large thinning factor was required. An estimate of the acceptance rate is provided by *cosmomc*.

4.2.4 THE LIKELIHOOD FUNCTION

The heart of the MC code is the likelihood function, that guides the random walk towards regions of high probability. The function (see Appendix D for details) calculates the χ^2 between the observed spectrum² μ and the spectrum at a given

²Because the observations are actually given by a set of n spectra (one for each radial bin), the final χ^2 is taken as the average over the individual χ_i^2 of the annuli. The

point in the parameter space $f(par_1...par_n)$:

$$\chi^2 = \sum_i \frac{(f_i(par) - \mu_i)^2}{\sigma_i^2} \quad (4.3)$$

where the sum is taken over the energy bins and σ_i^2 is the standard error on the count rate for the i -th channel. When using simulated observations, the errors are modeled as Poissonian noise $\sigma_i \propto \sqrt{N_i}$, with N_i being the number of photons detected in the i -th channel. A different choice of σ^2 would make the distribution more (or less) peaked around the central value: this possibility is explored further in Fig 4.6a.

4.3 CALCULATING THE SPECTRUM

It's important now that we find an efficient way to calculate a large number of spectra. As seen in Chapter 2.3.1, Xspec has a built-in code to reproduce spectra from an X-ray source, but it would be extremely time consuming having to run Xspec for each Metropolis step. Instead, I want to try to find a fast way to compute numerically the spectrum, with good approximation, with no need to call Xspec.

What makes it so hard to find a simple expression for the spectrum, is its characteristic irregular shape, with spikes and line features that are impossible to reproduce through simple analytical functions. All these complicated features are described by the cooling function $\Lambda(T)$.

This is the moment to start looking at things from a different angle. Rather than plotting the spectrum as a function of energy, like we usually do, we can fix the energy and slowly change the temperature. As it turns out (Figure 4.3), the signal is a rather regular function of the temperature and these profiles can be easily fitted by a simple expression. For a given energy $E = h\nu$ one can write, to a very good approximation,

$$f(T, \nu) = a_\nu T^3 + b_\nu T^2 + c_\nu T + d_\nu \quad (4.4)$$

where all terms beyond T^3 are negligible. Equation (4.4) provides a rather good fit, that can be further improved by fitting separately low- and high-temperature regions, the border between the two being at 3 keV. In this way, I obtain two sets of parameters, that are displayed in Figure 4.4.

Then I can reconstruct the cooling function in the range of interest by applying equation (4.4). For simplicity, the spectrum was given per unitary density: setting the density back to its correct value would only change the normalization

differences from the χ^2 in 4.3 are minimal.

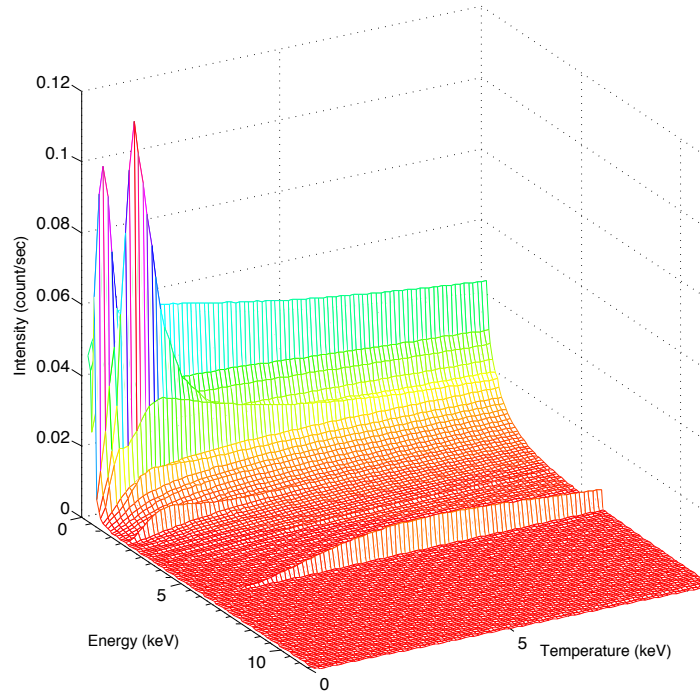


Figure 4.2: A family of spectra $f(T, E)$ when the temperature of the plasma is allowed to vary from $T = 0.1$ to 11 keV, showing that the function is much more regular along a section of constant energy than along a section of constant temperature. If we take a slice of constant temperature, let's say T_1 , we find a spectrum f_{T_1} , with some complicated features that are impossible to fit. This is especially visible at low temperature, where line emission is the dominant process. On the other hand, profiles of constant energy, f_E , are very smooth and can be fitted easily. Examples of two-dimensional slices are shown in Fig. 4.3. The actual calculations were done with 10 times more points than shown in this figure.

by a factor n_e^2 (eq. (1.2)). Of course, the approximation is not perfect and cannot be extrapolated outside the fitting range³, but, at this stage, speed is more important than extreme precision. The high energy part of the spectrum (above 8keV) proved to be more difficult to reproduce, and would require a better fit. For testing purpose, the energy range has been restricted to 0.3 – 7.5 keV. A comparison between the ‘correct’ spectrum (from Xspec) and the approximate one is shown in Figure 4.5.

These spectra can be projected along the line of sight to mimic observations of a cluster. The way of doing so is analogous to what is described in Chapter 3.6: I assume that each shell is isothermal and make a wighted sum over all the

³The fitting range was chosen to match the range where *Chandra* is operative, namely $0.2 \div 10$ keV.

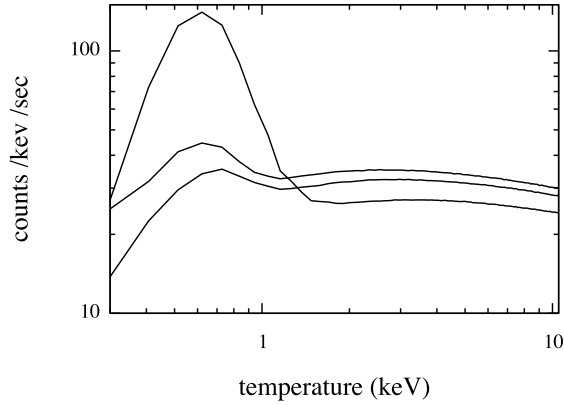


Figure 4.3: Sections of the function $f(T, E)$ for constant values of E , with a resolution of ~ 0.1 keV or 10^3 points. The values were extracted from Xspec's *mekal* model and interpolated with eq. (4.4).

cells along the line of sight.

4.3.1 THE RESPONSE FUNCTION

To be sure that I'm not introducing any systematics by mixing spectra with different response, I do not wish to apply the response matrix until the very last stage (i.e., just before comparison with observations). In this way, the procedure has the advantage of being detector independent, so that it could potentially be applied to data other than *Chandra's* only by replacing the response files. The procedure used to extract the files from Xspec is described in Appendix B.

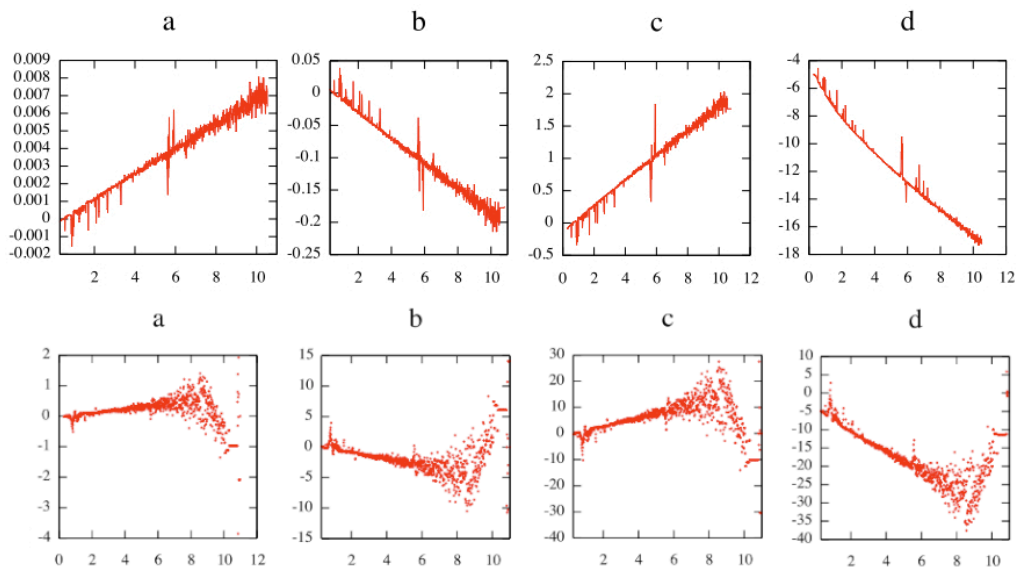


Figure 4.4: Fit parameters $\{a, b, c, d\}$ as function of energy. The upper set holds for temperatures above 3 keV (*top*), the bottom one for temperatures below 3 keV. At low temperature the spectra are dominated by line emission, which causes the fit parameters to be more scattered.

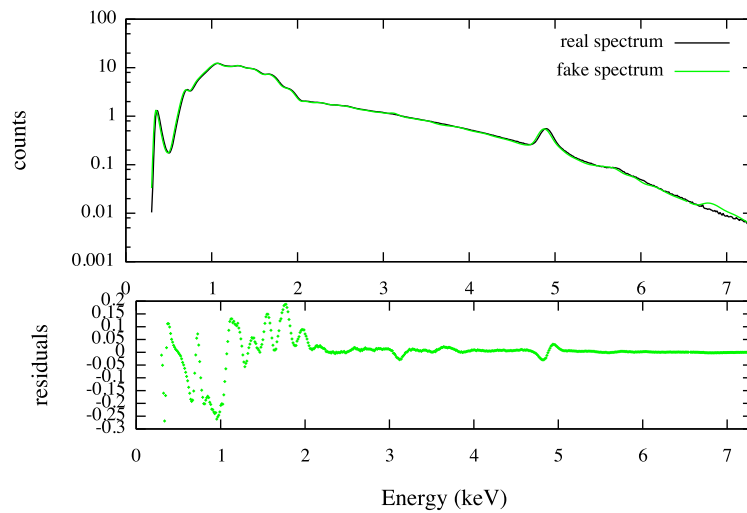


Figure 4.5: A comparison between a ‘real’ spectrum and its approximation reconstructed in the way outlined in Chapter 4.3. *Top:* a model spectrum of a $T = 4\text{keV}$ plasma made with Xspec (in black) together with the same spectrum calculated with equation (4.4) and (1.2) and convolved with *Chandra*’s response files (in green). *Bottom:* residual plot highlighting the differences between the real spectrum and its approximation (in linear scale to show the negative values). For the worst points, errors are still well contained within 1%.

4.4 TESTING

Again, I want to test the method on a simple model, that keeps the number of free parameter to a minimum. I start by parametrizing a simple cluster, like the one used in Section 3.7, with single power-law temperature and density profile:

$$T(r) = T_0 \left(\frac{r}{r_0}\right)^{-a} \quad \text{and} \quad n_e(r) = n_0 \left(\frac{r}{r_0}\right)^{-b} \quad (4.5)$$

The cluster has a spherical core and is prolate at large radii ($\alpha = 1$, $\beta = 1$). As a first test, I fix all the parameters but the one defining the shape (α), which I try to fit. The Monte Carlo quickly converges to the solution, that is $\alpha_{min} = 1.00 \pm 0.49$. The shape of the one-dimensional χ^2 Figure 4.6a is somewhat reminiscent of the results obtained with the deprojection in Chapter 3.7 et seq. (see figure 3.11 for a comparison).

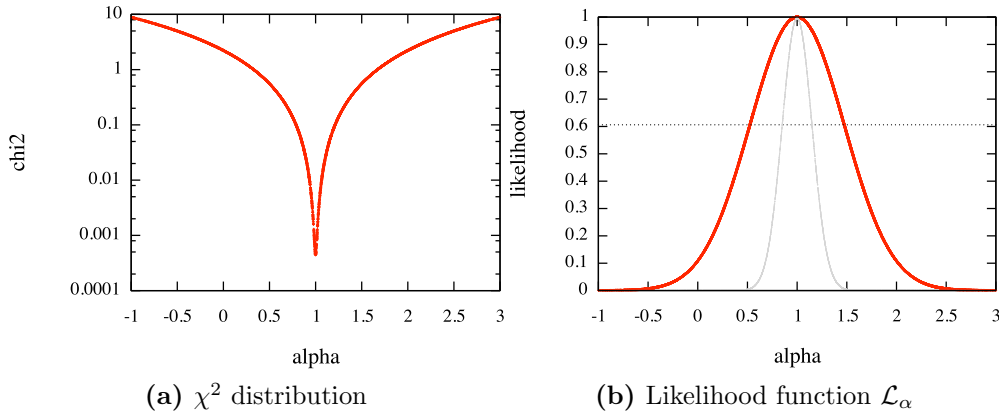


Figure 4.6: (a) χ^2 distribution for the parameter α from a one-dimensional Monte Carlo run used as a test. The curve is symmetrical, with a minimum in the χ^2 found for $\alpha_{min} = 1.00 \pm 0.49$. (b) Likelihood function (in red) with 1σ contours (dotted line). In light grey is shown how the probability would change if we reduce the errorbars on the observations by a factor 10.

The next step is to fit all the parameters in equation 4.5, starting from the temperature and the density slopes. From the distribution of points after a long run we can obtain the full probability distribution (Fig. 4.7), that can be marginalized over to find the most-probable parameter estimates. The parameters mean values after 20 000 Monte Carlo steps are shown in Table 4.1.

Note that most of the expectation values contain the real value, although the relative errors are as big as 30%. The contour plot, however, reveals a complicated parameter space. The density seems to be especially badly constrained. Moreover, the results are sensitive to the parameter space volume available.

parameter	mean	real value
a	1.22 ± 0.37	1
b	0.91 ± 0.25	1.2
α	0.66 ± 0.15	0.5

Table 4.1: Expectation values (with standard deviation) of the model parameters, after 20 000 Monte Carlo steps. The real values are shown for comparison.

Unfortunately, these results cannot immediately be extended to more complicated distributions, nor this procedure could be directly applied to the data. At the moment, fit to complicated models with a larger number of parameters are difficult to constrain and do not converge to the correct values. This should be improved by tuning carefully the error in 4.3 and the step size of each parameter.

4.5 WHAT'S NEXT?

In this thesis, I explored the possibility that clusters elongation can be investigated from the analysis of their spatially resolved X-rays observations. The effect of different geometries should be primarily seen as a small change in the exponential cut-off of the spectrum, due to the temperature gradient in the cluster volume. Throughout the work, I made the assumption, widely used in literature [3, 19, 30], that clusters can be thought of as an onion-like structures, made of concentric layers of constant temperature and density. I restricted the analysis to the special class of spheroidal clusters aligned with the line of sight, but it would be interesting to extend the description to full triaxial geometries. For simplicity, I also assumed that the ellipticity of the cluster evolves linearly with the radius (eq. 3.5), but, in the future, the effect of higher order terms should be considered.

I attempted to solve the problem in two complementary ways: the first method was based on a deprojection (or ‘onion peeling’) of the observational data, while the second method starts by projecting a 3D model of the cluster and then runs an optimization procedure.

The deprojection, described in Chapter 3, has been applied to *Chandra*’s data (observations and simulations), providing a guess for the cluster profile and ellipticity. However, the effect proved to be so small that, in the case of A2218 and A1689, the ellipticity was impossible to constrain. Nevertheless, working on simulations, where the signal-to-noise ratio was not an issue, confirmed the idea that the specific geometry of the cluster does indeed affect the overall X-ray emission. We also learned that the effect is less pronounced, and therefore more difficult to detect, in clusters with a flat or peaked temperature profile, as in

cool-core clusters.

In Chapter 4 I dropped the deprojection algorithm and tried instead to optimize a (projected) model until agreement with the data was reached. This second method is parametric, and it therefore requires that we can make a reasonable guess for the cluster's profile. At the time being, it has only been applied to simple clusters with a power-law profile. Before proceeding further, the interpolation of the spectra should be refined (Ch. 4.3), especially in the high energy range.

The plan for the future is to test this procedure extensively against more complicated gas distributions, including double power law and cored profiles, in the way done in Chapter 3.7 and following. One could also improve the way the projections are done, by considering a larger number of shells, or, in the most correct scenario, integrating the emission along the line of sight, as from eq. (3.1), rather than summing discrete volume elements. Then, ideally, the procedure should be applied to observational data. The fact that the response matrices are treated separately would make the procedure suitable to data other than *Chandra's*. Once we have a reliable estimate of the ellipticity, this could be used to improve our understanding of clusters cosmology. In particular, if SZ data for the cluster were available, one could use them to derive the Hubble constant.

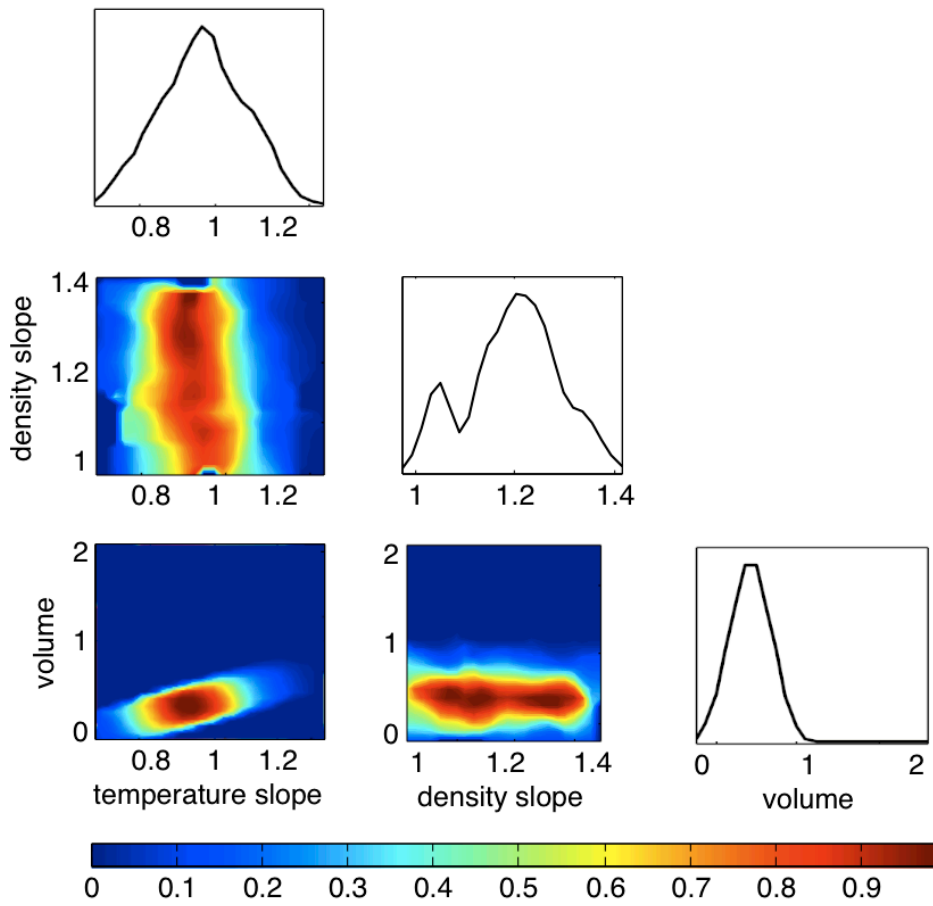


Figure 4.7: Contour plots for a prolate cluster model with three free parameter, after a MC run. The color scale is the probability of each point, red being high probability regions and blue low probability. For each parameter the marginalized distribution is also shown (solid black profiles).

Appendices

APPENDIX A

Deprojection of Abell 2218

Abell 2218 is a cluster at redshift $z = 0.175$ that is famous for being a powerful gravitational lens. Similarly to the case of A1689, masses deduced from X-rays are bigger by roughly a factor two than masses from X-rays [35]: among possible explanations to this discrepancy, there would be a possibility that the cluster is indeed not spherical. Other reasons include non-thermal contributions to the gas pressure from magnetic fields and bulk motions. Here I want to verify the hypothesis of non-sphericity using the method described in Chapter 3, the non-spherical deprojection of the cluster.

I follow the same procedure used in Chapter to analyze A1689 (Chapter 3.10). The deprojected temperature and density profiles are shown below in Figure A.1a, together with a plot of the χ^2 (Fig. A.1b). The results are not dissimilar from what found for A1689: again, it seems that the deprojected profiles are too noisy to be fitted with the required accuracy.

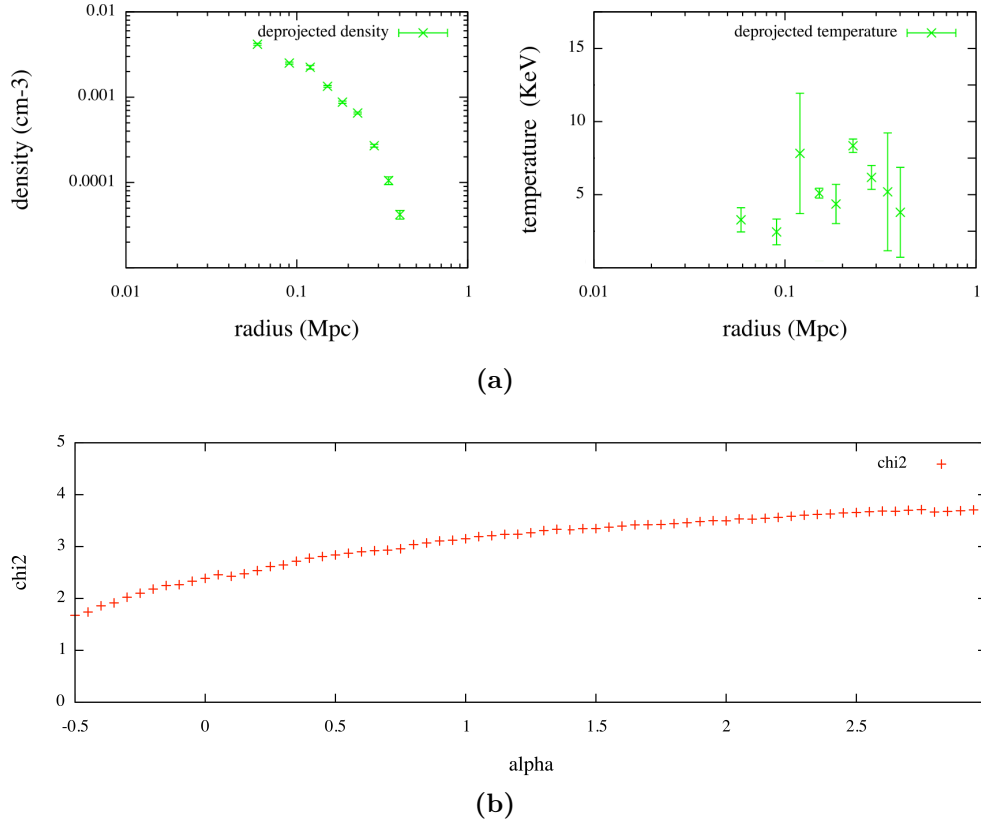


Figure A.1: (a) Results of the deprojection of Abell 2218. *Left:* best fit density profile, in cm^{-3} . *Right:* best fit temperature profile, in keV . Fitting the spectrum with the theoretical *mekal* model including galactic absorption yields a gas average temperature of $T = 5.7 \pm 1.2 \text{ keV}$. (b) The χ^2 distribution as a function of the shape coefficient α . Again, variations in the χ^2 are minimal (see Fig. 3.14 for comparison), with a mild preference cluster for geometries that are rather spherical (if not oblate) at large radii. There is no minimum on α : beyond the lower bound $\alpha = -0.5$, the parametrization becomes unphysical.

APPENDIX B

Extracting the response files

As discussed in Chapter 2.2, all the information about the detector response is stored in two files: a two-dimensional redistribution matrix (*wrmf*), containing the detector gain and energy resolution, and the one-dimensional ancillary response file (*arf*), containing the detector efficiency.

The response depends on the position on the detector and can vary in a non-predictable way with time, therefore it's important that every data file has its own response matrix. In my case, each observation was split in 10 – 15 rings, so there were as many response files. To be sure that I'm working under the most general assumptions and that I'm not introducing any systematics by summing up spectra with different response files, I do not include the response files until the very last stage (i.e., just before comparison with observations). In this way, I also make sure that the procedure is detector independent and thus can be applied to data from several telescopes.

B.1 THE SPECTRAL RESPONSE

In order to minimize disk-space requirements, these files are in a compressed format where all matrix elements below a threshold (of 10^{-6} keV) are considered zero and are not stored [21]. The compressed file contains long arrays of non-zero elements, together with informations about their position in the original matrix. The expression 'channel subset' indicates a group of contiguous channels for which the matrix elements are above the threshold. The organization of the data within the *wrmf* file is shown in Figure ???. Each row corresponds to a single energy range and consists of the following columns:

1. E_{low} : containing the lower energy bound of the energy bin,
2. E_{high} : the upper energy bound of the energy bin,
3. N_{grp} : the number of 'channel subsets' for the energy

Extension
to *(filename).RMF*
Name: RMF
Description: Photon Redistribution Matrix
Format: BINTABLE

1	2	3	column 4	5	6
<i>contents</i> Low energy bound for row	High energy bound for row	Number of channel subsets for row	First channel in each subset for row	Number chans in each subset for row	(non-zero) Matrix elements for row
E_{low}	E_{high}	N_{grp}	$F_{chan}(i)$ $i = 1, N_{grp}$	$N_{chan}(j)$ $j = 1, N_{grp}$	$Mat(k)$ $k = 1, \sum_{j=1}^{N_{grp}} N_{chan}(j)$
<i>format of each column</i>					
4-byte real	4-byte real	2-byte integer	2-byte integer array	2-byte integer array	4-byte real array
<i>total number of elements per row</i>					
1	1	1	variable, or MAX(N_{grp})	variable, or MAX(N_{grp})	variable, or MAX($\sum_{j=1}^{N_{grp}} N_{chan}(j)$)
<i>column name</i>					
ENERG_LO	ENERG_HI	N_GRP	F_CHAN	N_CHAN	MATRIX

Figure B.1: How the response matrix looks like: the FITS format for storing photon redistribution matrices within a *wrmf*. From the *Calibration requirements for spectral analysis* [21].

4. F_{chan} : a vector (of integers) telling the channel number of the start of each channel subset' for the energy bin,
5. N_{chan} : another integer vector, containing the number of elements within each channel subset for the energy bin,
6. *Matrix*: a real vector, containing the response values for each channel subset for the energy bin.

Each row is normalized to one detected photon, i.e. each element of the matrix is the probability of a photon in the energy range (E_{min} , E_{max}) giving rise to a signal in that channel. As they represent probabilities, the matrix elements are dimensionless.

The content of the response files can be accessed through a visualization program like *fv* from the Ftool package. I exported the data from the original FITS format (the standard format used by Nasa) to an ASCII file. Then, I wrote a Matlab routine to reconstruct the full matrix including the zero entries. Using the notation above, a given row in the *Matrix* array contains elements:

$$F_{chan}(1) \rightarrow (F_{chan}(1) + N_{chan}(1) - 1)$$

followed by:

$$\begin{aligned}
 F_{chan}(2) &\rightarrow (F_{chan}(2) + N_{chan}(2) - 1) \\
 F_{chan}(3) &\rightarrow (F_{chan}(3) + N_{chan}(3) - 1) \\
 &\dots \\
 F_{chan}(N_{grp}) &\rightarrow (F_{grp}(N_{grp}) + N_{chan}(N_{grp}) - 1)
 \end{aligned}$$

Every other entry is set to zero.

B.2 THE ANCILLARY RESPONSE

The ancillary response *arf* files are relatively straightforward to treat. They consist of a simple one-dimensional vector containing the product of all the components (effective area, filter transmission, correction factors, etc) as a function of energy. The data are in units of cm^2 .

The *arf* can be visualized using the command *plot efficiency* in Xspec, and then printed to an ordinary ASCII file.

Once the spectral and ancillary response have been restored, applying them to a data file is just a matter of matrix multiplication. If S is the real spectrum of the source, the detected spectrum S^* can be found as

$$S^*(i) = \sum_{E_j} R(i, E_j) A(E_j) S(E_j) \quad (\text{B.1})$$

where R and A are the spectral and ancillary response, respectively. The i 's indicate the detector energy channels and the E_j 's are the incoming photon energies.

APPENDIX C

The Hubble constant

A brief description of use of the Sunyaev-Zel'dovich effect as a cosmological probe was given in Chapter 1.6. The basic idea is that the distance to the cluster depends on a comparison of the X-ray emission and CMBR absorption of radiation from the gas. The results presented were introduced in a paper by Birkinshaw and Hughes [10] and later generalized for non-spherical clusters [9].

The emission from the gas in a cluster of galaxies is measured by its X-ray surface brightness, and is proportional to the line of sight integral of some density squared,

$$E \propto \int n_e^2 dl \quad (\text{C.1})$$

while the absorption of a background source of radiation is measured by the thermal Sunyaev-Zel'dovich effect, whose intensity is proportional to the optical depth,

$$A \propto \int n_e dl \quad (\text{C.2})$$

Thus, if both the emission from the gas, E , and its absorption, A , can be measured, the quantity A^2/E is a density weighted measure of the path length through the gas. If the structure of the gas is known and its angular size, θ , can be measured, then the angular diameter distance of the gas can be estimated as $A^2/(E\theta)$. Here, the density is assumed to be uniform: things get more complicated if there is clumping¹.

Since the technique compares the angular size of the cluster (θ) with a measure of the line of sight size of the cluster (A^2/E), it's important to have a realistic model for the inner structure of the gas. It's convenient to express the

¹The 'clumpiness' of the gas is measured by the coefficient $C_n = \langle n_e^2 \rangle / \langle n_e \rangle^2$ [9]. Since the X-ray emission depends on the average of n_e^2 , while the SZ depends on an average of n_e , the overall effect is sensitive to variations in C_n .

electron density and temperature in terms of a central value and a dimensionless form factor, describing the angular structure of the gas density and temperature. The angular variables are the angle from the line of sight, θ ; the angle from the line of sight through the cluster center, $\xi = l/d_A$, and the azimuthal angle about the line of sight, ϕ . d_A is the angular diameter distance of the cluster. Then the electron density and temperature at some location, r , are

$$n_e(r) = n_{e,0} f_n(\theta, \xi, \phi) \quad (\text{C.3})$$

$$T_e(r) = T_{e,0} f_T(\theta, \xi, \phi) \quad (\text{C.4})$$

and we can rewrite the cooling function $\Lambda(T)$ in terms of similar form factors, which depend on f_n and f_T in a complicated way,

$$\Lambda(T) = \Lambda_0 f_\Lambda(\theta, \xi, \phi) \quad (\text{C.5})$$

And the same can be done for the spectrum function,

$$\Psi(T) = \Psi_0 f_\Psi(\theta, \xi, \phi) \quad (\text{C.6})$$

The X-ray surface brightness and the thermal Sunyaev-Zel'dovich effect can then be expressed in terms of physical constants and angular structure, as

$$S_X(\theta, \phi) \equiv N_X \Theta_1(\theta, \phi) \quad (\text{C.7})$$

$$\Delta I(\theta, \phi) \equiv N_{SZ} \Theta_2(\theta, \phi) \quad (\text{C.8})$$

where $N_X = \frac{\Lambda_0 n_{e,0}^2 d_A}{4\pi(1+z)^3}$ and $N_{SZ} = \Psi_0 I_0 n_{e,0} \sigma_T d_A$ contain all the relevant physical informations, while all the structural information is contained into the angles

$$\Theta_1(\theta, \phi) = \int f_n^2 f_\Lambda d\xi \quad (\text{C.9})$$

$$\Theta_2(\theta, \phi) = \int f_n f_\Psi d\xi \quad (\text{C.10})$$

The absolute distance to the cluster is then found by fitting the X-ray and Sunyaev-Zel'dovich effect data to models of the form of equation C.7 to deduce N_X and N_{SZ} , and calculating the angular diameter distance using

$$d_A = \left(\frac{N_{SZ}^2}{N_X} \right) \left(\frac{\Lambda_{e,0}}{4\pi(1+z)^3 I_0^2 \Psi_0^2 \sigma_T^2} \right) \quad (\text{C.11})$$

and the value of the Hubble constant can be obtained from the measured redshift of the cluster and the value of d_A .

If the model for f_n is modified to make the cluster atmosphere prolate or oblate, then the apparent X-ray and Sunyaev-Zel'dovich images will be ellipsoidal, of circular if the symmetry axis lies along the line of sight. In this last

case the core radius of gas along the line of sight is larger by a factor $q = c/a$ than the core radii in the other two directions (c and a being, as usual, the major and minor semiaxis). The expression for Θ_1 and Θ_2 remains valid, while the normalization N_X and N_{SZ} both increase by a factor q . The result is that a prolate axis distribution with the symmetry along the line of sight.

Such clusters give biased estimates of the distance, since the true angular diameter distance is

$$d_A(true) = \frac{d_A(estimated)}{q} \quad (C.12)$$

if the distance is estimated using equation C.11 under the assumption of spherical symmetry.

APPENDIX D

My code

In this section I will describe the content of the code I have written to simulate the model clusters and do the deprojection in Chapter 3 and to do the Monte Carlo simulation in Chapter 4.

The actual code can be found here: http://bit.ly/code_Martina.

D.1 DEPROJECTION

This is a list of the code used to perform a non-spherical deprojection as described in Chapter 3. The scripts are written in *tcl*, as they are meant to be run within Xspec.

common.tcl A short *tcl* script that extracts fit results, including χ^2 , from Xspec and writes them to a *tcl* variable.

sphvol.tcl An Xspec function to calculate the cell volumes of an ellipsoid, given the array or radii and the relation between major and minor axis from equation (3.6).

genspectra.tcl This is the program used to create a 3D model cluster and project it along the line of sight. First it creates n spectra from hot diffuse gas using Xspec's *mekal* model and some temperature profile, that is also defined within the script. Then, each shell is weighted according to (3.11), giving the spectra of the 2D observational annuli.

peelingfake.tcl This is the Fortran program that performs the actual deprojection. Takes as input a set of observational spectra (like those constructed in the previous step) and tries to recover density, temperature and ellipticity of each 3D shell. It loops over different values of α , returning for each step the fit parameters and the χ^2 . Finally, finds the value of α that minimize the χ^2 and prints the best fit parameters.

peeling.tcl Is similar to **peelingfake.tcl**, but meant to be used with real observations, rather than Xspec fake data. Except for minor details, the program follows exactly the same path seen before: loops over the values of α (and eventually β), does the deprojection and returns the best fit 3D temperature profile and density profile. Also returns the χ^2 as a function of α and estimates the most probable value of α .

D.2 PROJECTIONS AND MONTE CARLO

Here is a list of files used to extract the cooling function from Xspec's *mekal* code and simulate a model cluster. The idea behind this method is explained in Chapter 4.3.

params.f90 Configuration file. Contains all the numbers relative to the observation: number of detector channels, energy range, number of annuli, etc.

fakespec.tcl Xspec command file to produce a large number of spectra (~ 100) with constant density and slowly increasing temperature. All spectra have unitary response.

profile.f90 This is a Fortran program that takes the output from **fakespec.tcl** and cuts a slice through each energy channel, in this way obtaining ~ 1000 profiles as function of the temperature.

fit.C This is a ROOT routine that perform a 3rd degree polynomial fit in equation (4.4) to the temperature profiles. Fits separately low-temperature profiles (0.3 – 3 KeV) and high-temperature (3 – 15 KeV). Saves the results to a Fortran module.

copy_to_camb.sh Copies all the relevant file to the Cosmomc folder.

fakec.tcl Configuration file, containing the relevant cluster properties (redshift, abundance) and information about the observation, such as exposure time, number of channel, number of annuli. . . . Its content can be re-written in Fortran-friendly format by running **write_params.tcl** .

xspepro.tcl An Xspec command file to simulate the theoretical X-ray emission from a cluster. Contains the definition of the density and temperature profiles. The instrumental response is set to *dummy*, to simulate a perfect detector. The resulting spectra are written to an ASCII data file.

xspepro.f90 Fortran program to project 3D shells into observational annuli, as described in equation (3.11). The resulting spectra are written to a

single Fortran module and copied to the `cosmomc` folder, where they are used as ‘observations’.

Finally, here is the content of the Monte Carlo code I have used to optimize the projected spectra, as described in Chapter 4. I only list the programs and subroutines written by me, while the actual Monte Carlo code can be found online [33].

xigar.f90 It’s the heart of the MC code as it contains the definition new likelihood function (*xraylike*), that I substituted to the standard one used by *cosmomc*. Basically, the function evaluates the spectra at each MC step using equation (4.4) and (1.2). Then those spectra are compared to the observations by using equation (4.3). To ensure that the comparison makes sense, the synthetic spectra are multiplied by the correct response matrices (contained in **response_matrix.f90**)

sphvol.f90 It’s just the Fortran analog for **sphvol.tcl**. Using the current value of α and equation (3.6), calculates the cells volumes to be used in the projections.

params_xray.ini Input file for *cosmomc*. Contains the number of free parameters, with starting point, upper and lower limits, and step size for each one. Also contains the total number of steps and length of the burn-in phase.

D.3 RESPONSE MATRICES

response.m A Matlab program that loads the compressed *wrmf* response file, together with the vectors containing N_{grp} , F_{chan} , and N_{chan} and reconstructs the full matrix. Then, each channel by its efficiency (from the *arf* file). The results are printed the to a data file.

apply_response.m Applies the response to a real spectrum and compares with the observations.

Bibliography

- [1] Heasarc catalog. Online at <http://heasarc.gsfc.nasa.gov/>.
- [2] G. O. Abell. The Distribution of Rich Clusters of Galaxies. *Astrophysical Journal Supplement* , 3:211–+, May 1958.
- [3] S. Ameglio, S. Borgani, E. Pierpaoli, and K. Dolag. Joint deprojection of Sunyaev-Zeldovich and X-ray images of galaxy clusters. *MNRAS* , 382:397–411, November 2007.
- [4] E. Anders and M. Ebihara. Solar-system abundances of the elements. *Geochimica et Cosmochimica Acta*, 46, November 1982.
- [5] K. E. Andersson and G. M. Madejski. Complex Structure of Galaxy Cluster A1689: Evidence for a Merger from X-Ray Data? *ApJ* , 607:190–201, May 2004.
- [6] K. A. Arnaud, B. Dorman, and C. Gordon. Xspec, an x-ray spectral fitting package. user’s guide for version 12.5.1. Technical report, NASA/GSFC, August 1998.
- [7] E. S. Battistelli, M. De Petris, L. Lamagna, G. Luzzi, R. Maoli, A. Melchiorri, F. Melchiorri, A. Orlando, E. Palladino, G. Savini, Y. Rephaeli, M. Shimon, M. Signore, and S. Colafrancesco. Triple Experiment Spectrum of the Sunyaev-Zel’dovich Effect in the Coma Cluster: H_0 . *ApJ Lett.* , 598:L75–L78, December 2003.
- [8] J. Binney and S. Tremaine. *Galactic Dynamics*. Princeton University Press, 2008.
- [9] M. Birkinshaw. The Sunyaev-Zel’dovich effect. *Physics Reports* , 310:97–195, March 1999.
- [10] M. Birkinshaw, J. P. Hughes, and K. A. Arnaud. A measurement of the value of the Hubble constant from the X-ray properties and the Sunyaev-Zel’dovich effect of Abell 665. *ApJ* , 379:466–481, October 1991.

-
- [11] H. Boehringer and N. Werner. X-ray Spectroscopy of Galaxy Clusters. *ArXiv e-prints*, July 2009.
- [12] S. Borgani and A. Kravtsov. Cosmological simulations of galaxy clusters. *ArXiv e-prints*, June 2009.
- [13] D. A. Buote and J. C. Tsai. Quantifying the Morphologies and Dynamical Evolution of Galaxy Clusters. I. The Method. *ApJ* , 452:522–+, October 1995.
- [14] A. Cavaliere and R. Fusco-Femiano. The Distribution of Hot Gas in Clusters of Galaxies. *AAP* , 70, November 1978.
- [15] M. Colless, G. Dalton, S. Maddox, W. Sutherland, P. Norberg, S. Cole, J. Bland-Hawthorn, T. Bridges, R. Cannon, C. Collins, W. Couch, N. Cross, K. Deeley, R. De Propris, S. P. Driver, G. Efstathiou, R. S. Ellis, C. S. Frenk, K. Glazebrook, C. Jackson, O. Lahav, I. Lewis, S. Lumsden, D. Madgwick, J. A. Peacock, B. A. Peterson, I. Price, M. Seaborne, and K. Taylor. The 2dF Galaxy Redshift Survey: spectra and redshifts. *MNRAS* , 328:1039–1063, December 2001.
- [16] V. L. Corless and L. J. King. An MCMC fitting method for triaxial dark matter haloes. *MNRAS* , 390:997–1013, November 2008.
- [17] P. A. M. de Theije, P. Katgert, and E. van Kampen. The shapes of galaxy clusters. *MNRAS* , 273:30–46, March 1995.
- [18] X. Er and P. Schneider. Estimate of dark halo ellipticity by lensing flexion. *ArXiv e-prints*, September 2010.
- [19] S. Ettori. Projection effects in X-ray cores of cooling flow galaxy clusters. *MNRAS* , 330:971–976, March 2002.
- [20] I. George. The mathpha users guide. Technical report, NASA/GSFC, August 1997.
- [21] I. George and K. A. Arnaud. The calibration requirements for spectral analysis. definition of rmf and arf formats. Technical report, NASA/GSFC, December 1998.
- [22] C. P. Haines, G. P. Smith, M. J. Pereira, E. Egami, S. M. Moran, E. Hardegree-Ullman, T. D. Rawle, and M. Rex. LoCuSS: Shedding new light on the massive lensing cluster Abell 1689 - the view from Herschel. *AAP* , 518:L19+, July 2010.
- [23] S. Ho, N. Bahcall, and P. Bode. Cluster Ellipticities as a Cosmological Probe. *ApJ* , 647:8–12, August 2006.

- [24] J. P. Hughes and M. Birkinshaw. A Measurement of the Hubble Constant from the X-Ray Properties and the Sunyaev-Zeldovich Effect of CL 0016+16. *ApJ* , 501:1–+, July 1998.
- [25] P. Humphrey, D. Buote, F. Gastaldello, and L. Zappacosta. LMXBs And Globular Clusters In Early-type Galaxies. In *AAS/High Energy Astrophysics Division #9*, volume 38 of *Bulletin of the American Astronomical Society*, pages 377–+, September 2006.
- [26] P. J. Humphrey, D. A. Buote, F. Brighenti, K. Gebhardt, and W. G. Mathews. Weighing the Quiescent Central Black Hole in an Elliptical Galaxy with X-Ray-Emitting Gas. *ApJ* , 683:161–171, August 2008.
- [27] Y. P. Jing and Y. Suto. Triaxial Modeling of Halo Density Profiles with High-Resolution N-Body Simulations. *ApJ* , 574:538–553, August 2002.
- [28] P. M. W. Kalberla, W. B. Burton, D. Hartmann, E. M. Arnal, E. Bajaja, R. Morras, and W. G. L. Pöppel. The Leiden/Argentine/Bonn (LAB) Survey of Galactic HI. Final data release of the combined LDS and IAR surveys with improved stray-radiation corrections. *AAP* , 440:775–782, September 2005.
- [29] H. Kawahara, T. Kitayama, S. Sasaki, and Y. Suto. Systematic Errors in the Hubble Constant Measurement from the Sunyaev-Zel’dovich Effect. *ApJ* , 674:11–21, February 2008.
- [30] G. A. Kriss, D. F. Cioffi, and C. R. Canizares. The X-ray emitting gas in poor clusters with central dominant galaxies. *ApJ* , 272:439–448, September 1983.
- [31] D. Lenze, R. Barkana, T. J. Broadhurst, and Y. Rephaeli. Mass and gas profiles in A1689: joint X-ray and lensing analysis. *MNRAS* , 386:1092–1106, May 2008.
- [32] A. Lewis and S. Bridle. Cosmological parameters from CMB and other data: A Monte Carlo approach. *Phys. Rev. D*, 66(10):103511–+, November 2002.
- [33] Antony Lewis. Cosmological monte carlo, May 2010. Available at <http://cosmologist.info/cosmomc/>.
- [34] M. Limousin, J. Richard, E. Jullo, J.-P. Kneib, B. Fort, G. Soucail, Á. Elíasdóttir, P. Natarajan, R. S. Ellis, I. Smail, O. Czoske, G. P. Smith, P. Hudelot, S. Bardeau, H. Ebeling, E. Egami, and K. K. Knudsen. Combining Strong and Weak Gravitational Lensing in Abell 1689. *ApJ* , 668:643–666, October 2007.

- [35] G. Madejski, K. Andersson, J. Peterson, and P. Marshall. Complex structure of galaxy clusters Abell 1689 and Abell 2218. In *Bulletin of the American Astronomical Society*, volume 36 of *Bulletin of the American Astronomical Society*, pages 1202–+, August 2004.
- [36] N. et al. Metropolis. Equation of State Calculations by Fast Computing Machines. *J. Chem. Phys.*, 21, 1953.
- [37] R. Mewe, E. H. B. M. Gronenschild, and G. H. J. van den Oord. Calculated X-radiation from optically thin plasmas. V. *Astronomy and Astrophysics Supplement Series*, 62:197–254, November 1985.
- [38] A. Morandi, S. Ettori, and L. Moscardini. X-ray and Sunyaev-Zel’dovich scaling relations in galaxy clusters. *MNRAS* , 379:518–534, August 2007.
- [39] Morrison and McCammon. Interstellar photoelectric absorption cross sections, 0.03-10 keV. *ApJ* , 270, 1983.
- [40] M. Plionis, J. D. Barrow, and C. S. Frenk. Projected and intrinsic shapes of galaxy clusters. *MNRAS* , 249, April 1991.
- [41] M. Plionis, J. D. Barrow, and C. S. Frenk. Projected and intrinsic shapes of galaxy clusters. *MNRAS* , 249:662–677, April 1991.
- [42] P. P. Plucinsky, N. S. Schulz, H. L. Marshall, C. E. Grant, G. Chartas, D. Sanwal, M. Teter, A. A. Vikhlinin, R. J. Edgar, M. W. Wise, G. E. Allen, S. N. Virani, J. M. DePasquale, and M. T. Raley. Spectral response of the ACIS instrument. In J. E. Truemper & H. D. Tananbaum, editor, *Society of Photo-Optical Instrumentation Engineers (SPIE) Conference Series*, volume 4851 of *Society of Photo-Optical Instrumentation Engineers (SPIE) Conference Series*, pages 89–100, March 2003.
- [43] Signe Riemer-Sørensen. *Dark Matter Characterization From X-ray Observations*. Ph.D. thesis, Dark Cosmology Center, Niels Bohr Institute, August 2009.
- [44] G. Rhee, M. van Haarlem, and P. Katgert. A study of the elongation of Abell clusters. II - A sample of 107 rich clusters. *Astronomy and Astrophysics Supplement Series*, 91, December 1991.
- [45] C. L. Sarazin. Book-Review - X-Ray Emissions from Clusters of Galaxies. *Sky Telescope* , 76, December 1988.
- [46] L. S. Sparke and S. Gallagher. *Galaxies in the Universe*. Cambridge University Press, 2007.
- [47] L. Spitzer. *Physics of Fully Ionized Gas*. Wiley, 1961.

-
- [48] R. A. Sunyaev and I. B. Zeldovich. Microwave background radiation as a probe of the contemporary structure and history of the universe. *Annual Review of Astronomy and Astrophysics* , 18, 1980.
- [49] A. Vikhlinin, A. Kravtsov, W. Forman, C. Jones, M. Markevitch, S. S. Murray, and L. Van Speybroeck. Chandra Sample of Nearby Relaxed Galaxy Clusters: Mass, Gas Fraction, and Mass-Temperature Relation. *ApJ* , 640, April 2006.
- [50] G. M. Voit. Tracing cosmic evolution with clusters of galaxies. *Reviews of Modern Physics*, 77, April 2005.
- [51] W. Vetterling W. H. Press, S. Teukolsky and B. Flannery. *Numerical recipes in Fortran 77*. Cambridge University Press, 2007.
- [52] S. D. M. White, J. F. Navarro, A. E. Evrard, and C. S. Frenk. The baryon content of galaxy clusters: a challenge to cosmological orthodoxy. *Nature* , 366:429–433, December 1993.
- [53] S.-J. Xue and X.-P. Wu. Chandra X-Ray Observatory Observation of A1689: New Determination of Mass Distribution and Comparison to Lensing Measurements. *ApJ* , 576, September 2002.